

Seasonal and latitudinal variations of surface fluxes at two Arctic terrestrial sites

**Andrey A. Grachev, P. Ola G. Persson,
Taneil Uttal, Elena A. Akish,
Christopher J. Cox, Sara M. Morris,
Christopher W. Fairall, et al.**

Climate Dynamics

Observational, Theoretical and
Computational Research on the Climate
System

ISSN 0930-7575

Volume 51

Combined 5-6


Clim Dyn (2018) 51:1793-1818

DOI 10.1007/s00382-017-3983-4



Your article is protected by copyright and all rights are held exclusively by Springer-Verlag GmbH Germany. This e-offprint is for personal use only and shall not be self-archived in electronic repositories. If you wish to self-archive your article, please use the accepted manuscript version for posting on your own website. You may further deposit the accepted manuscript version in any repository, provided it is only made publicly available 12 months after official publication or later and provided acknowledgement is given to the original source of publication and a link is inserted to the published article on Springer's website. The link must be accompanied by the following text: "The final publication is available at link.springer.com".

Seasonal and latitudinal variations of surface fluxes at two Arctic terrestrial sites

Andrey A. Grachev^{1,2}  · P. Ola G. Persson^{1,2} · Taneil Uttal¹ · Elena A. Akish^{1,3} · Christopher J. Cox^{1,2} · Sara M. Morris^{1,2} · Christopher W. Fairall¹ · Robert S. Stone^{1,3} · Glen Lesins⁴ · Alexander P. Makshtas⁵ · Irina A. Repina⁶

Received: 19 April 2017 / Accepted: 16 October 2017 / Published online: 9 November 2017
© Springer-Verlag GmbH Germany 2017

Abstract This observational study compares seasonal variations of surface fluxes (turbulent, radiative, and soil heat) and other ancillary atmospheric/surface/permafrost data based on in-situ measurements made at terrestrial research observatories located near the coast of the Arctic Ocean. Hourly-averaged multiyear data sets collected at Eureka (Nunavut, Canada) and Tiksi (East Siberia, Russia) are analyzed in more detail to elucidate similarities and differences in the seasonal cycles at these two Arctic stations, which are situated at significantly different latitudes (80.0°N and 71.6°N, respectively). While significant gross similarities exist in the annual cycles of various meteorological parameters and fluxes, the differences in latitude, local topography, cloud cover, snowfall, and soil characteristics produce noticeable differences in fluxes and in the structures of the atmospheric boundary layer and upper soil temperature profiles. An important factor is that even though higher latitude sites (in this case Eureka) generally receive less annual incoming solar radiation but more total daily incoming solar radiation throughout the summer months than lower

latitude sites (in this case Tiksi). This leads to a counter-intuitive state where the average active layer (or thaw line) is deeper and the topsoil temperature in midsummer are higher in Eureka which is located almost 10° north of Tiksi. The study further highlights the differences in the seasonal and latitudinal variations of the incoming shortwave and net radiation as well as the moderating cloudiness effects that lead to temporal and spatial differences in the structure of the atmospheric boundary layer and the uppermost ground layer. Specifically the warm season (Arctic summer) is shorter and mid-summer amplitude of the surface fluxes near solar noon is generally less in Eureka than in Tiksi. During the dark Polar night and cold seasons (Arctic winter) when the ground is covered with snow and air temperatures are sufficiently below freezing, the near-surface environment is generally stably stratified and the hourly averaged turbulent fluxes are quite small and irregular with on average small downward sensible heat fluxes and upward latent heat and carbon dioxide fluxes. The magnitude of the turbulent fluxes increases rapidly when surface snow disappears and the air temperatures rise above freezing during spring melt and eventually reaches a summer maximum. Throughout the summer months strong upward sensible and latent heat fluxes and downward carbon dioxide (uptake by the surface) are typically observed indicating persistent unstable (convective) stratification. Due to the combined effects of day length and solar zenith angle, the convective boundary layer forms in the High Arctic (e.g., in Eureka) and can reach long-lived quasi-stationary states in summer. During late summer and early autumn all turbulent fluxes rapidly decrease in magnitude when the air temperature decreases and falls below freezing. Unlike Eureka, a pronounced zero-curtain effect consisting of a sustained surface temperature hiatus at the freezing point is observed in Tiksi during fall due to wetter and/or water saturated soils.

✉ Andrey A. Grachev
andrey.grachev@noaa.gov

¹ NOAA Earth System Research Laboratory, 325 Broadway, R/PSD3, Boulder, CO 80305-3337, USA
² Cooperative Institute for Research in Environmental Sciences, University of Colorado, Boulder, CO, USA
³ Science and Technology Corporation, Boulder, CO, USA
⁴ Department of Physics and Atmospheric Science, Dalhousie University, Halifax, NS, Canada
⁵ Arctic and Antarctic Research Institute, St. Petersburg, Russia
⁶ A.M. Obukhov Institute of Atmospheric Physics, Russian Academy Sciences, Moscow, Russia

Keywords Arctic · Carbon dioxide · Latitudinal variations · Radiative fluxes · Turbulent fluxes

1 Introduction

The Arctic region is experiencing unprecedented changes associated with increasing average temperatures (faster than the pace of the globally-averaged increase) and significant decreases in both the areal extent and thickness of the Arctic pack ice (e.g., McBean et al. 2005; Serreze et al. 2007; Stroeve et al. 2007; Overland et al. 2008; Kaufman et al. 2009; Walsh et al. 2011; Polyakov et al. 2012 and references therein). Regional Arctic temperature changes show foci of annual warming along the coast of northeastern Siberia and the Canadian Archipelago (Overland et al. 2011), while numerous studies show a recent wintertime “warm Arctic—cold continent” pattern; that is, warming foci along the Siberian Coast and the Canadian Archipelago and strong cooling over the Siberian interior (e.g., Overland et al. 2011; Kug et al. 2015; Sun et al. 2016). Terrestrial permafrost temperatures at long-term permafrost monitoring sites in the high Canadian Arctic have increased since 2000 at a rate of +0.4° to +1.2 °C/decade, though slight cooling has been seen at a few sites during recent years (Romanovsky et al. 2016). Thickening of the summertime active layer in northern Siberia has been continuous from 1999 to 2012, with little change or small thinning in the three most recent years (Romanovsky et al. 2016). The increase in atmospheric carbon dioxide, an important greenhouse gas, has raised concerns about global impacts of Arctic climate change (e.g., Oechel et al. 2000, 2014; Baldocchi et al. 2001; Laurila et al. 2001; Harazono et al. 2003; Kwon et al. 2006; Mbufong et al. 2014 and references therein). Some studies suggest that huge stores of carbon dioxide (and other climate relevant compounds) locked up in Arctic soils could be released due to permafrost thawing, and would act as a positive feedback to climate change (e.g., Oechel et al. 2000; Mbufong et al. 2014). These and other changes suggest shifts in the global climate system that justifies increased scientific focus on this region.

Observational evidence suggests that atmospheric energy fluxes are a major contributor to the decrease of the Arctic pack ice, seasonal land snow cover and the warming of the surrounding land areas and permafrost layers (e.g., Stone 1997; Stone et al. 2002; Laxon et al. 2003; Francis et al. 2005; Persson 2012). To better understand the atmosphere-surface exchange mechanisms, improve models, and to diagnose climate variability in the Arctic, accurate measurements are required of all components of the surface energy budget (SEB) and the carbon dioxide cycle over representative areas and over multiple years. Knowing which flux components are the major contributors to the observed changes allows us

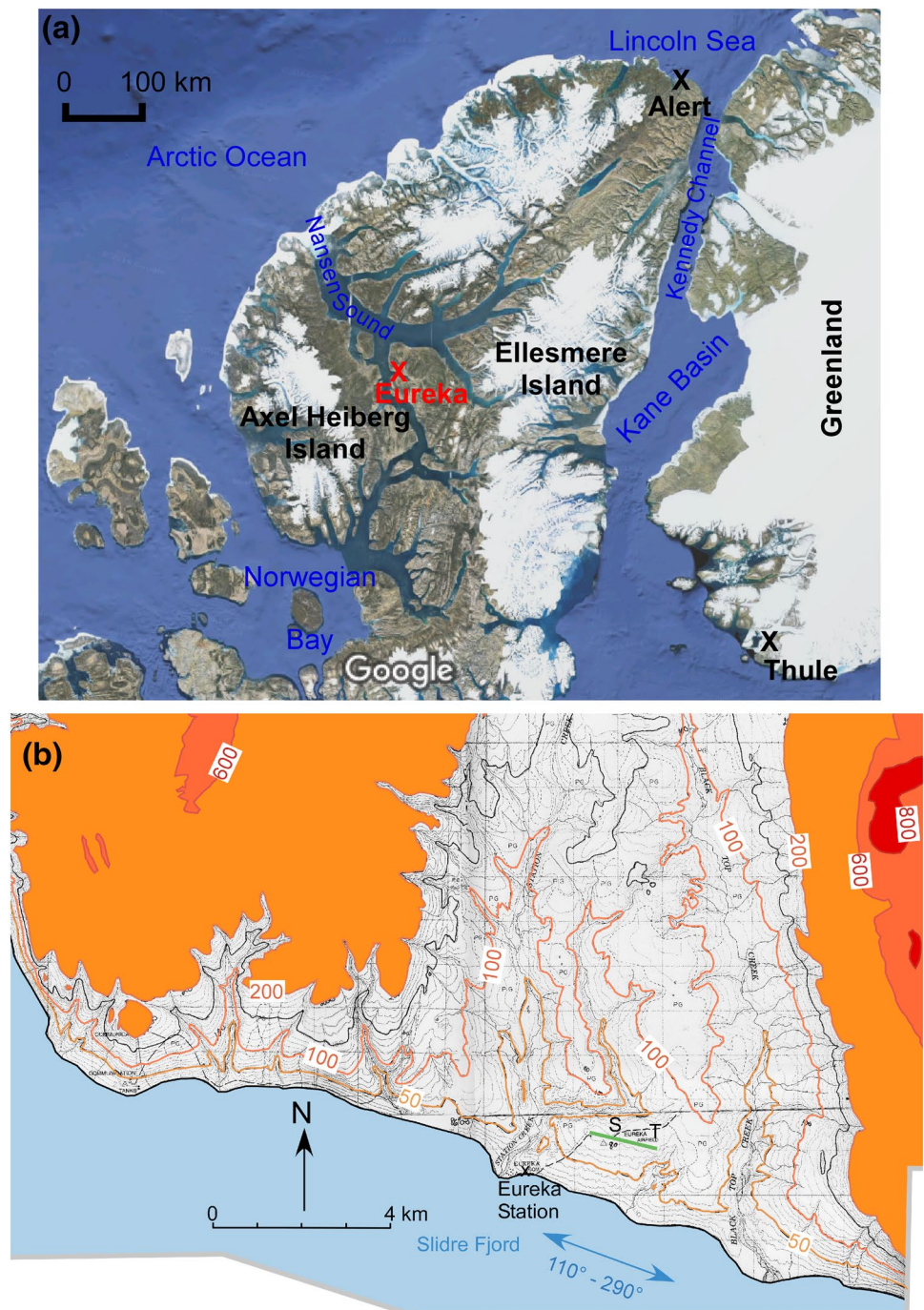
to attribute the changes to specific physical processes, and possibly determine the role, if any, of anthropogenic effects (Serreze et al. 2007). Once the fundamental processes are quantified and understood, we can evaluate current model performance and improve key parameterizations needed to predict future climate change.

This study presents cross-disciplinary, multi-year observations of the surface energy fluxes at two long-term Arctic observatories, providing understanding of key processes producing the annual energy cycle at each site and also of those producing clear differences between these two high-latitude sites. The two sites, located at different latitudes and in different ecosystems, are Eureka (80.0°N) on Ellesmere Island, Nunavut, Canada (Fig. 1a) and Tiksi, Russia (71.6°N) located on the coast of the Laptev Sea (Fig. 2a). Both sites are in areas recording significant warming of near-surface air and permafrost temperature over the past decades, and changes in active-layer depth. In addition, Tiksi is located in the zone of large gradient in the wintertime temperature change associated with the “warm Arctic-cold continent” pattern. Furthermore, the location of Tiksi is also associated with summer Arctic frontal zone, a narrow band of strong horizontal temperature gradients spanning the coastlines of Siberia, Alaska, and western Canada that extends through a considerable depth of the troposphere (Crawford and Serreze 2015). Hourly averaged turbulent and radiative near-surface energy fluxes and conductive ground fluxes are examined, in addition to the thermal evolution in the atmospheric boundary layer and within the soil. Hence, the evolution of the soil active layer and permafrost characteristics are linked to soil and atmospheric energy fluxes and to key processes and environmental characteristics throughout the annual cycle, including effects of clouds, snow cover, soil moisture and soil characteristics. The carbon dioxide fluxes measured at both sites are used for establishing baseline measurements of fluxes of this greenhouse gas for future use in documenting potential changes associated with permafrost changes, and for linking CO₂ fluxes to physical processes associated with the energy fluxes.

2 Observation sites and instrumentation

To monitor and better understand causes for observed changes in the Arctic regions, a number of agencies and institutions in the Arctic countries (Canada, Russia, US, Finland, Denmark, Norway) often in collaboration with other non-Arctic countries (China, Japan, Germany, and others) have established a number of long-term, intensive, atmospheric observatories around the Arctic Basin. Primary long-term observation sites are Alert and Eureka, Canada; Barrow, USA; Tiksi, Russia; Ny-Ålesund (Svalbard), Norway; and Summit (Greenland), Denmark; these

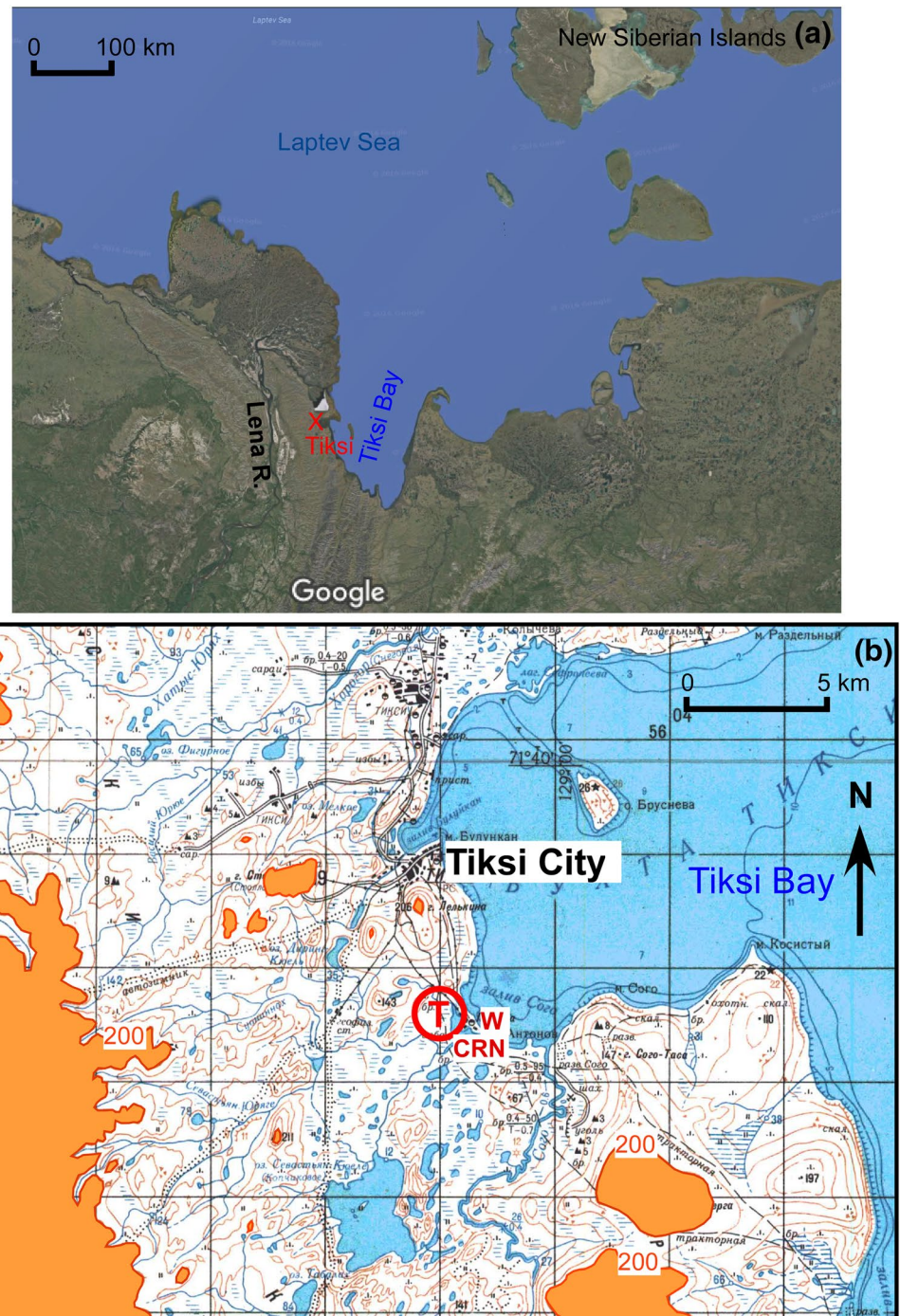
Fig. 1 Maps showing the Eureka region: **a** Ellesmere Island and the surrounding area, including the few development sites. Eureka is marked by a red “X”. White areas primarily show ice caps, which have altitudes of 1000–2000 m. Coastal white shows permanent ice shelves (adapted from Google Maps); **b** topographic map of the region near the long-term Eureka Station, located on the shore of the Slidre Fjord. Symbols “T” and “S” show the locations of the flux tower and downwelling radiation site (SAFIRE), respectively, both located ~200 m north of the gravel runway (green line). Terrain contours are in meters, and altitudes > 200 m are shaded



observatories are members of a consortium (International Arctic Systems for Observing the Atmosphere (IASOA), <http://www.iasoa.org>) that coordinates observing strategies, data sharing and support for science collaboratories (Uttal et al. 2016). Here we analyze observations from Eureka and Tiksi to investigate the annual cycle of the surface fluxes and their link to atmospheric processes. Although some measurements made at these sites were analyzed previously (see references below), the turbulent fluxes and other data collected at these sites are reported

here for the first time. Original data used in the current study are publicly available. Access to the datasets (‘raw data’ and ‘final products’) and time series of various variables (data browser) are available through the IASOA Data Portal for Arctic atmospheric measurements (<https://www.esrl.noaa.gov/psd/iasoa/dataataglance>) (Starkweather and Uttal 2016) and/or the NSF Arctic Data Center (<https://arcticdata.io/>) and/or the NOAA Earth Systems Research Laboratory Physical Science Division Arctic data archives

Fig. 2 Maps showing the Tiksi region: **a** the Lena River Delta and the surrounding area. Tiksi city is marked by a red “X” (adapted from Google Maps); **b** the Tiksi tower location is marked by the red, encircled “T” ~ 700 m from Tiksi Bay and at ~ 5–10 m altitude. Symbols “W” and “CRN” show the long-term Tiksi weather station and the Climate Research Network site, respectively, both located ~ 1.5 km SE of the tower. Terrain contours are in meters, and altitudes > 200 m are shaded



(<https://www.esrl.noaa.gov/psd/arctic/observatories/index.html>). Results have been also disseminated to education community through the outreach activities to bring relevant Arctic climate research into classrooms for high school students (Gold et al. 2015). Below we provide relevant information about these observation sites, instrumentation, measurements, and data processing (see also Uttal et al. 2013, 2016 for further details).

2.1 Eureka observatory

Eureka (80.05°N, 86.42°W) is a long-term research observatory on the Fosheim Peninsula of Ellesmere Island, the northernmost island in the Canadian Arctic Archipelago in the territory of Nunavut (Fig. 1). The facility is operated by a consortium of Canadian university and government researchers operating under the umbrella of the Canadian Network for Detection of Atmospheric Change ([Springer](http://</p>
</div>
<div data-bbox=)

www.candac.ca) with support from Environment Canada. It is located about 150 km inland from the Arctic Ocean within a complex network of fjords and mountains. The local area near the Eureka Station and the flux tower (see Fig. 1b) consists of the Slidre Fjord oriented WNW-ESE, a ~6–8 km broad valley extending northward with significant stream-carved topography of ~50–100 m in the valley floor, and two major ridges with tops at 600–900 m (Fig. 1b). Some taller mountains to the north, east and west of Eureka at a distance of 100–200 km are encased in ice caps. Eureka is well north of the treeline, and its main biome is tundra with significant amounts of flora and fauna compared to neighboring areas in the High Arctic. Eureka was established in 1947 as part of an Arctic weather station network, is one of two research stations on Ellesmere Island (Alert being the other), and weather observations have been archived since 1953. Lesins et al. (2010) use surface and sounding observations from the Eureka Station site along the shore of the Slidre Fjord to discuss some of the climatological conditions and trends, showing that a 0.9 °C per decade warming has occurred since 1972.

In the last 15 years, instrumentation at the site has been enhanced to monitor the changing Arctic climate. Beginning in 2004, remote sensors and other in-situ scientific instrumentation were installed at various locations near Eureka, including the Canadian Polar Environment Atmospheric Research Laboratory (PEARL) at 600 m elevation (on the western ridge in Fig. 1b) and a cloud radar, a lidar and microwave radiometer at the main Eureka Station. These data have been used to examine tropospheric cloud macro and microphysical properties at Eureka, as well as their radiative effects (Ishii et al. 1999; de Boer et al. 2008, 2009; Shupe 2011; Shupe et al. 2011; Mariani et al. 2012; Cox et al. 2012, 2014, 2015; and; Blanchard et al. 2017) and to show that moisture intrusion events into the High Arctic from lower latitudes impact the surface downwelling long-wave radiation (Doyle et al. 2011).

In 2007, the NOAA Earth System Research Laboratory (Physical Sciences Division) team and Environment Canada erected a 10.5-m flux tower and downwelling radiation sensors about 700 m apart at two sites (labelled “T” and “S”, respectively, in Fig. 1b) 200 m north of the runway at ~80 m altitude and ~2 km from the Slidre Fjord (see Fig. 1b). The instruments include, but are not limited to, surface flux instruments, a tropospheric ozone lidar and radiometric sensors. Downwelling shortwave and longwave radiometers at the Canadian Surface and Atmospheric Flux, Irradiance and Radiation Extension (SAFIRE, site “S” in Fig. 1b; also see Fig. 4 of Matsui et al. 2012) were part of the global Baseline Surface Radiation Network (BSRN) during the study period. Upwelling/downwelling shortwave and longwave radiation instruments are also located at the top of the flux tower (~10.5 m AGL); upwelling radiation was also measured for

a time at a separate “albedo mast” between “T” and “S”. The flux tower instruments include measurements of the following quantities: atmospheric pressure; profiles of temperature, humidity, and wind over the height of the tower; covariance turbulent fluxes of momentum, sensible heat, latent heat, and CO₂; surface snow depth and temperature; soil heat flux at two locations (“grass area” and “raised mud”); and temperature within the soil to a depth of 1.2 m. A complete list of instrumentation near the flux tower is given in Table 1. Figure 3a shows the instrumentation on the Eureka flux tower, while Fig. 4a shows the area near the base and to the NNW of the tower. The tower is oriented at about 350° (true north is 0°) so the sonic anemometer booms at 3.07 and 7.54 m are oriented towards 256° and 79°, respectively. With these orientations and the boom lengths, useful data is obtained simultaneously from both sonic anemometers for airflow from all directions except 79°–123° and 215°–259°, which only occurs 18% of the time (Fig. 5a). Given the configuration of the anemometer and the observed wind rose, useful wind and turbulence profiles are available 82% of the time at the Eureka flux tower. These tower-based eddy covariance measurements provide a long-term near continuous temporal record of hourly average mass and energy fluxes.

The mean wind speed and wind direction were derived from the sonic anemometers, with rotation of the anemometer axes needed to place the measured wind components in a streamline coordinate system based on 1-h averaged 10-Hz data. We used the most common method, which is a double rotation of the anemometer coordinate system, to compute the longitudinal, lateral, and vertical velocity components in real time (Kaimal and Finnigan 1994, Sect. 6.6). The ‘fast’ 10-Hz raw data collected by a sonic anemometer were first edited to remove spikes from the data stream. Turbulent covariance and variance values were then derived through frequency integration of the appropriate cospectra and spectra computed from 54.61-min data blocks (corresponding to 2¹⁵ data points) from the original 60-min data files. Sonic anemometers measure the so-called ‘sonic’ temperature, which is close to the virtual temperature (e.g., Grachev et al. 2005, p. 205). A moisture correction is necessary to convert the sonic temperature to thermodynamic temperature in order to calculate sensible heat flux. Here this correction was performed following Schotanus et al. (1983). A fast-response (10 Hz) open path infrared gas analyzer LI-7500 (LI-COR Inc.) mounted on a boom at an intermediate level (about 6.75 m) just below the upper sonic anemometer is used for direct measurements of water vapor and carbon dioxide turbulent fluxes and other relevant turbulent statistics (see Table 1). Turbulent flux of carbon dioxide were computed based on the instantaneous mixing ratio of the trace gas relative to dry air according to the density correction theory of Webb et al. (1980, their Eq. 20). In the case of “fast” mixing ratio-based flux (i.e., converting the raw data point-by-point

Table 1 Instrumentation at Eureka

Flux tower: instrument description	Parameters	Height (m) ^a	Sampling rate	Time period of available data ^b
R.M. Young Wind Sentry Set (03001-L)	WS/WD	10.5	1 min	Sep 2007–present
Eppley PIR w ventilator	LW _d	10	1 min	Sep 2007–Jun 2012
Eppley PIR w ventilator	LW _u	10	1 min	Sep 2008–present
Kipp and Zonen high precision pyranometer (CM22) w ventilator	SW _d	10	1 min	Sep 2007–Jun 2012
Kipp nd Zonen high precision pyranometer (CM22) w ventilator	SW _u	10	1 min	Sep 2008–present
Vaisälä HMT337 T/RH probes—split T, hum probes, aspirated	T, RH	2, 6, 10	1 min	Sep 2007–present
RTD aspirated resistance temperature sensors	T	2, 6, 10	1 min	Sep 2008–present
Aspirated differential temperature thermocouples (CS ASPTC-L)	DT	2, 6, 6, 10	1 min	Sep 2007–present
ATI Sonic anemometers—K-style with heaters	u', v', w', T'	3.07, 7.54	10 Hz	Sep 2007–present
Licor LI-7500 open-path IR gas analyzer	q', CO ₂ '	6.75	10 Hz	Sep 2007–present
Campbell ultrasonic distance (snowdepth) sensor (SR50-L100)	H _{SN}	2.3	1 min	Sep 2007–present
Vaisälä PTB110 barometer (CS105)	P	2	1 min	Sep 2007–present
Apogee IR Thermocouple Sfc T sensor (CS IRTS-P)	T _s	3.2	1 min	Sep 2007–present
Averaging soil thermocouple probes (TCAV-L)	T _s	– 0.05	1 min	Sep 2007–present
Two Hukseflux soil heat flux plates (HFT3-L)	G	– 0.05	1 min	Sep 2007–present
Thermistor string (PT100)	T _{ss}	– 0.05 to – 1.2	1 min	Sep 2007–present
GPS-for time synchronization	t	–	Not recorded	Sep 2007–present
Tracker: instrument description	Parameters	Height (m)	Sampling rate	Time period of available data ^b
Eppley PIR w ventilator	LW _d	3	1 min	Mar 2008–present
Kipp nd Zonen high precision pyranometer (CM22) w ventilator	SW _d	3	1 min	Mar 2008–present
Albedo rack: instrument description	Parameters	Height (m)	Sampling rate	Time period of available data ^b
Eppley PIR w ventilator	LW _u	3	1 min	Jul 2012–present
Kipp and Zonen high precision pyranometer (CM22) w ventilator	SW _u	3	1 min	Jul 2012–present

^aHeight relative to local soil surface

^bTime period of data for analysis: 'data start date'—Dec 2014

to mixing ratios), the true turbulent flux of carbon dioxide can be expressed in pure eddy covariance form (see Grachev et al. 2011; Nakai et al. 2011 for discussion).

Several data-quality indicators based on objective and subjective methods have been applied to the original flux data in order to remove spurious or low-quality records. In particular, turbulent data have been edited for unfavorable relative wind directions, non-stationarity, mean wind vector tilt, and minimum or/and maximum thresholds for the turbulent statistics. Based on established criteria (see Grachev et al. 2013, 2015, 2016 and references therein for discussion), the following thresholds were used for this study to reject suspect data: To avoid a possible flux loss caused by inadequate frequency response and sensor separations, we omitted data with a local wind speed less than 0.2 m s⁻¹. We set minimum and/or maximum thresholds for the kinematic momentum flux (> 0.0002 m² s⁻²), vertical and along-slope temperature fluxes (< -0.0002 K m s⁻¹), standard deviation of each wind speed component (> 0.01 m s⁻¹), standard deviation of air temperature (> 0.01 K), vertical gradients of mean velocity (< -0.001 s⁻¹), dissipation rate of turbulent kinetic energy (0.00002 < ε < 0.1 m² s⁻³) and the dissipation

(destruction) rate for half the temperature variance (0.00002 < N_t < 0.01 K² s⁻¹). Points with excessive standard deviation of wind direction (> 30°), steadiness (trend) of the non-rotated wind speed components (Δu/U < 1, Δv/U < 1), and sonic temperature (> 2 °C) were also removed to avoid non-stationary conditions during a 1-h record. In addition, sonic anemometer angle of attack was limited by 10°.

Figure 5a shows the limited airflow regimes at the Eureka tower site. During winter, winds from 110°–160° occur most frequently and are associated with a downfjord flow along the Slidre Fjord from the ice-capped mountains to the ESE (see Fig. 1). These downfjord flows also occur in summer, as well as upfjord flow from the west after the snow has melted that represents a “sea-breeze” from the ice-covered Arctic Ocean 150 km to the NW. Occasionally during all seasons, there is also a drainage flow along a gully ~200 m to the NNW of the tower (see Figs. 1b, 4a). Large-scale synoptic forcing likely modulates these airflow regimes, though no studies have been conducted to show the linkage. An overview of climate statistics at Eureka for the period from 1954 to 2007 can be found in Lesins et al. (2010). A comparison of the atmospheric conditions at Eureka and Barrow is given

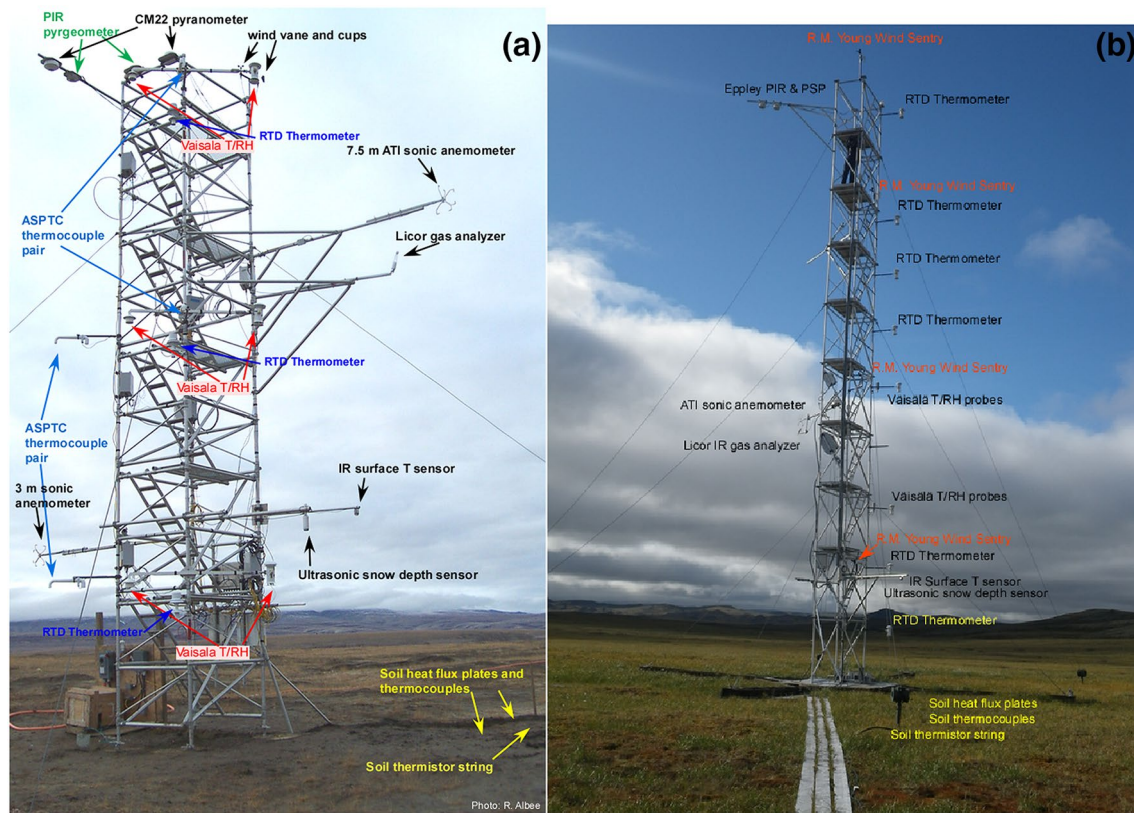


Fig. 3 Instrumentation and late summer conditions at the **a** Eureka flux tower (5 September 2008) and **b** the Tiksi flux tower (28 August 2012). Photo credits: **a** Robert Albee, NOAA, and **b** Vasily Kustov, Arctic and Antarctic Research Institute, St. Petersburg, Russia

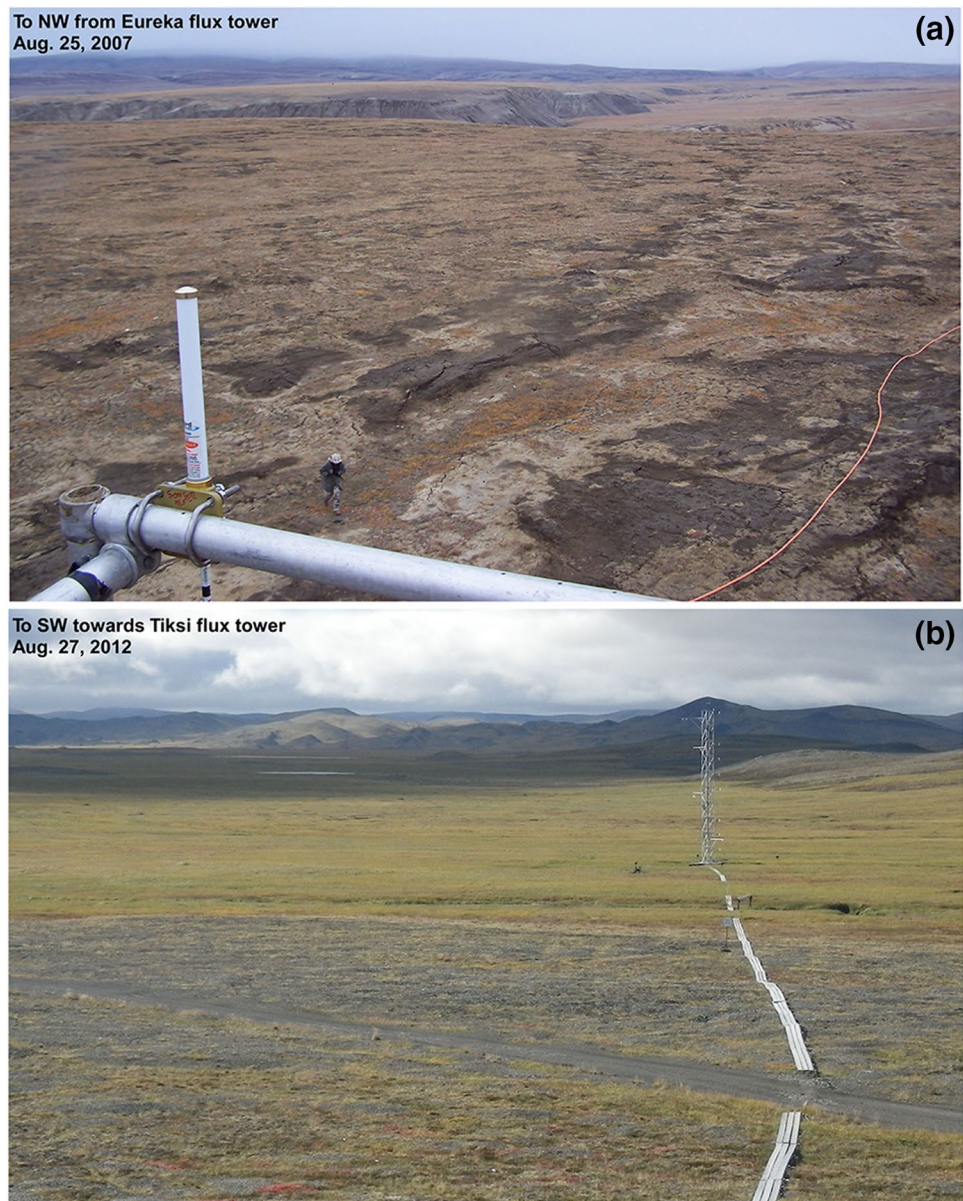
in Cox et al. (2012). Radiation measurements at Alert, Barrow, and Eureka in comparison with Boulder Atmospheric Observatory (Colorado) for 2008 are provided by Matsui et al. (2012). Other measurement of interest made at Eureka are described by Whyte et al. (2001), Lesins et al. (2009, 2012), Fast et al. (2011), and Cox et al. (2014).

2.2 Tiksi observatory

The Russian weather station at Tiksi, located in East Siberia (71.6°N, 128.9°E), was established at the Polyarka settlement on August 12, 1932 by the Russian Chief Management of the Northern Sea Route. The “Polyarka” observatory is located 7 km south of the town Tiksi, and is now the location of a new Hydrometeorological Observatory developed through a partnership between the Russian Federal Service for Hydrometeorology and Environmental Monitoring (Roshydromet), the US National Oceanic and Atmospheric Administration (NOAA), the Finnish Meteorological Institute, and the US National Science Foundation (NSF). This facility supports the research needs of the International community, is interdisciplinary, and includes Global Atmosphere Watch measurements as well as other climate observations (Uttal et al. 2013).

The site is located less than a kilometre from Tiksi Bay, which is a bay of the Laptev Sea SSW of the New Siberian Islands, and ~10 kilometres from a range of hills 200–400 m high to its WSW (Fig. 2). The main flux tower (see Fig. 3b) is 20 m in height and was erected and instrumented in summer 2010; regular turbulent measurements at the tower were started in April 2011 (Fig. 3b; Table 2). ‘Slow’ mean wind speed/direction, temperature, and humidity are measured at several heights between 1.8 m and 21 m with various instrument types (see Fig. 3b; Table 2 for details). Atmospheric pressure is measured at 5 m above the surface, surface (skin) temperature is measured by infrared sensor from 3.3 m, and snow depth is measured by a sonic sensor, the last two mounted at ~3.3 m height. Measurements of soil temperature in the active layer and permafrost are made by resistance temperature probes at 10 depths between the surface and 1.2 m. For measurements of soil heat flux at the surface in the vicinity of the soil temperature probes, two heat flux plates are buried at about 5 cm depth approximately 6 m north of the tower. Near-surface soil temperature around the heat flux plates is measured by averaging thermocouple probes. An additional heat flux plate is buried in the vicinity of the albedo rack.

Fig. 4 Photographs illustrating soil and vegetation conditions near the flux towers at **a** Eureka and **b** Tiksi. Both photographs show late summer conditions. Vegetation is evident at both sites, but is more lush with greater soil moisture at Tiksi. Photo credits: **a** Ola Persson and **b** Dmitry Apartsev



Upwelling longwave radiation is measured at the flux tower and also at a separate radiation mast (“albedo rack”) located NE of Polyarka weather station (W in Fig. 2b) (refer to Table 2). Upwelling shortwave radiation is only measured at the latter site. Downwelling longwave radiation is measured at the top of the flux tower and by the BSRN suite of instruments mounted on the roof of the Clean Air Facility (CAF) located approximately 315 m NW of the tower. Downwelling shortwave total, direct, and diffuse radiation are measured by a suite of radiometers and tracker on the CAF that are part of the BSRN.

Turbulent measurements at the tower are made by the identical three-axis ATI sonic anemometer/thermometers and a LI-COR open path infrared gas analyzer, all sampling at 10 Hz. Three sonic anemometers were originally mounted

at levels 3.3, 9.5, and 15.5 m, though only the two lower sonic anemometers are currently used. All sonic anemometers are oriented at about 197° (SSW) relative to true north. The gas analyzer is located at 9.3 m height, 0.2 m below the 9.5 m sonic anemometer. Data processing and data-quality control of the hourly averaged turbulent fluxes and other turbulent statistics are identical to the procedure described in the Sect. 2.1 for Eureka flux tower. One-minute ‘slow’-response data is averaged over an hour to be used together with the hourly turbulent fluxes. Because the two dominant wind directions are $\sim 180^\circ$ apart, the turbulent flux sensors positioned on one side of the tower are able to cleanly obtain profiles in all of the WSW flow and nearly all of the ENE flow (Fig. 5b). No turbulence data is obtained when winds are from 0° to 35° , which only occurs 3.6% of the time.

Fig. 5 Number of hourly mean wind speeds as a function of wind direction using all annual data at **a** Eureka for 2010 and **b** Tiksi for 2014. Wind speed and direction bins of 1 m s^{-1} and 10° were used. Wind directions for which sonic anemometers are blocked are delineated by the dashed black lines

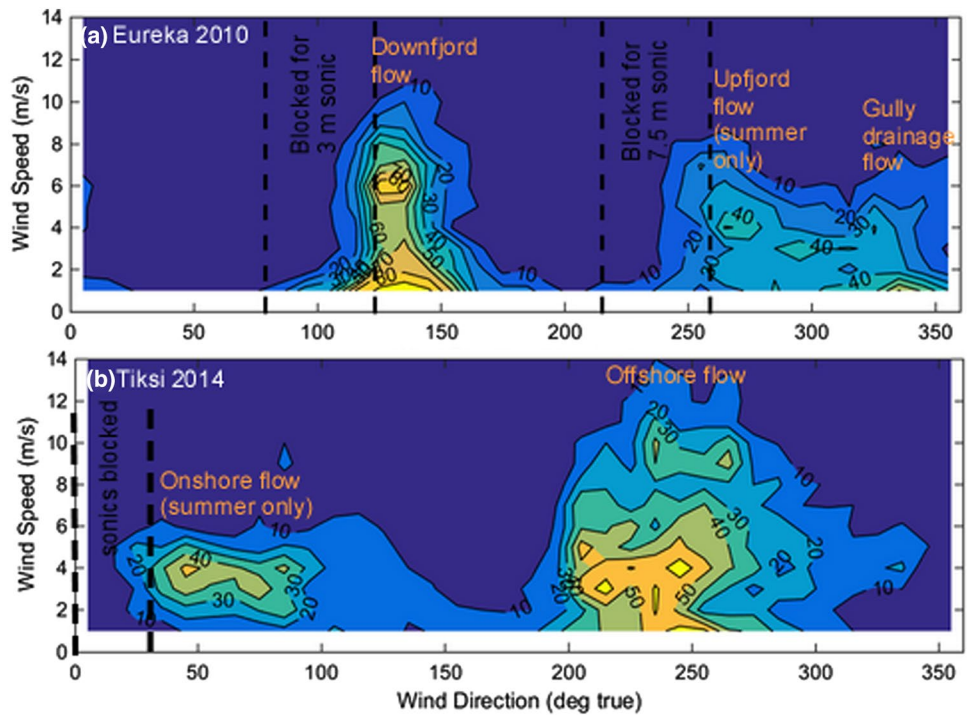


Table 2 Instrumentation at Tiksi

Flux tower: instrument description	Parameters	Height (m) ^a	Sampling rate	Time period of available data ^b
R.M. Young Wind Sentry Set (03001-L)	WS/WD	4, 9, 15, 21	1 min	Oct 2010–present
Eppley PIR w ventilator	LW _d	21	1 min	May 2011–present
Eppley PIR w ventilator	LW _u	21	1 min	May 2011–present
Väisälä HMT337/HMP155T/RH probes—split T, hum probes, aspirated	T, RH	2, 6,10	1 min	Oct 2010–present
RTD aspirated resistance temperature sensors	T	4, 8, 12, 14, 16, 20	1 min	Oct 2010–present
ATI Sonic anemometers—K-style with heaters	u', v', w', T'	3, 9	10 Hz	Apr 2011–present
Licor LI-7500 open-path IR gas analyzer	q', CO ₂ '	9	10 Hz	Apr 2011–present
Campbell ultrasonic distance (snowdepth) sensor (SR50A-L100)	H _{sn}	3.3	1 min	Oct 2010–present
Väisälä PTB110 barometer (PTB-110)	P	5	1 min	Oct 2010–present
Apogee IR Sfc T sensor(SI-III)	T _s	3.3	1 min	Oct 2010–present
Averaging soil thermocouple probes (TCAV-L)	T _s	– 0.05	1 min	Oct 2010–present
Two Hukseflux soil heat flux plates (HFP-01)	G	– 0.05	1 min	Oct 2010–present
Thermistor string (PT100)	T _{ss}	– 0.05 to -1.2	1 min	Oct 2010–present
GPS-for time synchronization	t		Not recorded	Oct 2010–present
Tracker: instrument description	Parameters	Height (m)	Sampling rate	Time period of available data ^b
Eppley PIR w ventilator	LW _d	3	1 min	Jun 2010–present
Kipp and Zonen high precision pyranometer (CM22) w ventilator	SW _d	3	1 min	Jun 2010–present
Albedo rack: instrument description	Parameters	Height (m)	Sampling rate	Time period of available data ^b
Eppley PIR w ventilator	LW _u	2	1 min	Apr 2011–present
Eppley PSP w ventilator	SW _u	2	1 min	Apr 2011–present

^aHeight relative to local soil surface

^bTime period of data for analysis: 'data start date'—Dec 2014

At the Tiksi tower site, the wind regimes are dominated by an offshore flow from 200° to 270° that is particularly persistent in winter (75% of time) as a cold, dry “land-breeze” effect (Fig. 5b). In summer (June 1–September 1), an ENE onshore flow occurs about as frequently as the offshore flow (~38% of time each), and represents a relatively cold, moist sea-breeze effect as the soil surface warms after the snow has melted. Long-term variability (1932–2007) of climate characteristics in the area of Tiksi Hydrometeorological Observatory is analyzed by Ivanov et al. (2009a, b), and Ivanov and Makshtas (2012). A detailed review of meteorological and permafrost conditions at Tiksi can be found in Romanovsky et al. (2007). Information of horizons of active layer, soil water regime, vegetation, and soil temperatures in tundra near Tiksi are available from Watanabe et al. (2000, 2003).

2.3 Error assessment

Error estimates for the various parameters and fluxes are needed to determine the validity of the interpretation of processes at each site and differences between the sites. While an error analysis based on multiple in-lab calibrations of the various instruments and on-site intercomparisons, such as that obtained for the SHEBA field program (Persson et al. 2002), is ideal, the availability of such calibrations and intercomparisons is limited for the Eureka and Tiksi deployments. The error estimates described below focus on Eureka, but they should be similar for Tiksi.

For the Eureka instruments, in-lab calibrations were done prior to deployment for some sensors, and the manufacturers’ settings were used for others. For several sensors,

the error estimates are just the manufacturers’ specifications. Comparisons of on-site measurements from identical instruments provide some quantification of instrument performance. Comparing vertical temperature differences from the Vaisala HMT337 probes with the occurrence of near-zero turbulent heat fluxes from the independent 7.54 m sonic anemometer indicates that the manufacturer’s specifications are correct, with small biases of ~0.05 °C, and random errors of ±0.2 °C (Table 3). Errors for the RTD temperature sensors are larger (not shown), making them less useful for providing vertical temperature profiles. Comparisons are also made of the sensible heat flux and friction velocity from the two sonic anemometers located at 3.07 and 7.54 m height on the flux tower. Classically, the constant flux layer of the atmospheric boundary layer is assumed to be the lowest 10% of the boundary layer; hence, all hours during 4 years (primarily summers of 2008, 2011–2014) were identified for which coincident good values were available from both sonic anemometers and for which the boundary layer was at least 100 m deep. The latter assessment used the classical Rossby–Montgomery formula (e.g., Appendix 3, Garratt 1992) which utilizes the measured friction velocity and the local Coriolis parameter and shown to be reasonable for Arctic conditions (Brooks et al. 2017), while the determination of “good” values includes restricting the wind direction to be outside the sectors impacted by airflow through the tower (see Fig. 5a). For these hours, the sensible heat flux and the momentum flux should theoretically be the same at both heights, so any differences are ascribed to either biases or random errors. Table 3 shows that the biases are small, consistent with the results from the SHEBA calibrations (Persson et al. 2002), though the random errors

Table 3 Eureka site error analysis. Estimates of biases and random (hourly and monthly) errors for selected parameters and fluxes

Parameters	Random errors (hourly)	Random errors (monthly)	Bias
T (HMT337)	± 0.2 °C	± 0.04 °C	± 0.05 °C
Specs	± 0.20–0.40 °C		
RH	Specs ± 1.8–3.0%		
Wind Speed	Specs ± 0.5 m s ⁻¹ , threshold 1.1 m s ⁻¹		
Wind Dir	Specs ± 5 deg		
SW _{down}	± 15.7 W m ⁻²	± 2.9 W m ⁻²	± 0.8 W m ⁻²
Specs	± 5%		
LW _{down}	± 10.8 W m ⁻²	± 2.0 W m ⁻²	± 0.3 W m ⁻²
Specs	± 5 W m ⁻²		
SW _{up}	± 5.0–8.6 W m ⁻²	± 0.9–1.5 W m ⁻²	± 1.3–3.1 W m ⁻²
LW _{up}	± 6.2 W m ⁻²	± 1.1 W m ⁻²	± 0.2–0.9 W m ⁻²
H _s	± 10.1 W m ⁻²	± 1.8 W m ⁻²	± 0.3 W m ⁻²
H _L	Specs 4–10%	n/a	n/a
u _*	0.042 m s ⁻¹	0.008 m s ⁻¹	± 0.015 m s ⁻¹
G	± 1–17 W m ⁻²	± 0.8–1.5 W m ⁻²	± 1 W m ⁻²
Specs	± 3%		

The specifications (specs) for some parameters indicated n/a mean “not available”

of the hourly sensible heat flux are estimated at 10 W m^{-2} , more than twice as large as at the SHEBA site. However, for longer timescales, the random errors are substantially less, estimated to be less than 2 W m^{-2} for monthly means and even smaller for annual means of the sensible heat flux. Since only one level of latent heat flux is measured, errors in these cannot be estimated in the same manner. Using specifications of errors for the sonic anemometer vertical wind component and the Licor 7500 moisture, a theoretical error in the latent heat flux of 4–10% is obtained.

On-site comparisons for the Eureka downwelling radiation is also possible, as this study only uses the radiation measurements at the flux tower. Coincident downwelling radiation measurements are available from the BSRN site at the SAFIRE location for 2009–2011 (see Table 1), and these were used to estimate potential biases and random errors. Because hourly averages are used, impacts of spatial differences caused by the 700 m separation should be small. Results suggest that biases are less than 1 W m^{-2} , while random hourly errors are 10.8 W m^{-2} for downwelling longwave radiation and 15.7 W m^{-2} (14%) for downwelling shortwave radiation (for downwelling shortwave, only scenes with at least 50 W m^{-2} irradiance measured at the flux tower were included in the analysis). Random errors for monthly means should be a factor of ~ 5.5 less, assuming independent daily radiative conditions. The estimates of the random radiation errors are larger at Eureka than for SHEBA, and may reflect greater impacts of riming on the sensors as the site receives daily rather than hourly maintenance as was the case at SHEBA. As for the temperature and turbulence error estimates above, these radiation error estimates are based on on-site instrument comparisons of two sensors, so errors in either or both instruments are included in these estimates. Comparisons between the upwelling longwave and shortwave radiation at the flux tower with upwelling radiation at the albedo rack is not possible because there was no overlap in time between the measurements. Error estimates of upwelling longwave radiation at sites at Alert and Barrow from similar instruments are ~ 0.2 – 0.9 and $\pm 6.2 \text{ W m}^{-2}$, which are shown in Table 3.

The instrument specifications suggest that the flux plate accuracy is $\pm 3\%$, which is about 1.5 W m^{-2} , though some studies suggest the errors might be substantially greater (e.g., up to 50%) due to issues of placement, soil thermal conductivity, contact between the soil and flux plate, etc. (e.g., Halliwell and Rouse 1987; Wang and Bou-Zeid 2012). The two flux plates that were within 5 m of each other near the base of the Eureka tower were intentionally placed in different soil types, with vegetation present for one and not for the other. This resulted in significant differences in the amplitudes and especially phasing of the diurnal soil flux signals in summer, with a July root-mean-square (RMS) difference of 17 W m^{-2} between the two. Despite this large

difference in the hourly signal, the monthly mean difference was only $\sim 1.5 \text{ W m}^{-2}$. In April, while snow cover was still present and vegetation was not yet active (the flux signals of the two plates should be very similar), the diurnal amplitude and phase differences were much muted and the RMS difference between the two plates was less than 1 W m^{-2} , similar to the mean difference. Hence, we estimate that the bias in the flux plate measurements is $\sim 1 \text{ W m}^{-2}$, with additional random errors of no more than the manufacturer's specifications of $\pm 3\%$ ($\sim 1.5 \text{ W m}^{-2}$). Significantly greater differences between summer flux plate measurements likely represent spatial heterogeneity in the actual ground flux rather than measurement errors, though errors from plate placement mentioned above can't be ruled out.

3 Annual cycles of the surface fluxes and surface meteorology

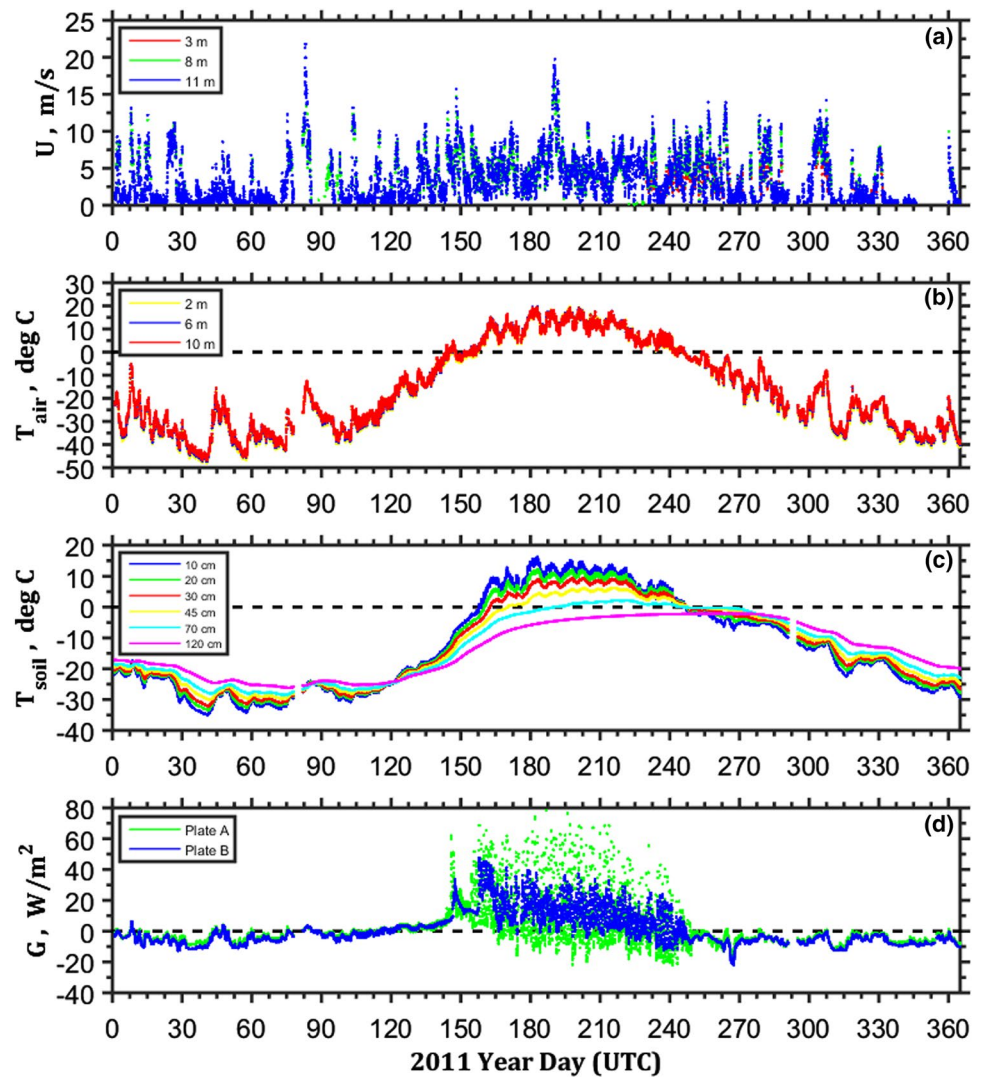
The annual cycles of basic meteorological parameters and key SEB components at Eureka are plotted in Figs. 6, 7 and 8. Figures 6 and 7 show a typical annual cycle of the 'slow' data: wind speed, air and soil temperature, soil heat flux, shortwave (SW) and longwave (LW) radiation (downwelling and upwelling), net radiation, R_{net} , and the surface albedo observed at Eureka during 2011. By convention, radiative fluxes are positive when directed toward the surface and fluxes away from the surface are negative. The net radiation is defined as the balance between downwelling (incoming) and upwelling (outgoing) SW and LW radiation:

$$R_{net} = SW_{down} - SW_{up} + LW_{down} - LW_{up}.$$

The surface albedo (reflectivity of a surface) in Fig. 7c is derived from the ratio of the upwelling SW radiation (i.e., reflected from the surface) to the downwelling SW radiation for a solar zenith angle (the angle between zenith and the Sun) $< 85^\circ$. The seasonal cycles of the turbulent fluxes of the sensible heat, latent heat, and carbon dioxide at Eureka during 2009–2012 and 2014 are shown in Fig. 8a–c. Figure 8d also shows difference of air virtual potential temperature between two levels to illustrate climatological (5 year) stratification of the atmospheric boundary layer (ABL) at Eureka, which plays an important role in the turbulent transfer of energy (cf. Fig. 8a–c). The data in Fig. 8 are based on 1-h (cyan x-symbols) and 5-day (blue solid lines) averaging of measurements. Similar time-series plots for Tiksi are shown in Figs. 9, 10 and 11 respectively. Note that the individual 1-h averaged points in Figs. 8 and 11 give an estimate of the available good data and the typical scatter of the data.

The annual cycles of the slow-response variables at the sites are plotted for a single year because they are very similar between the years that are analysed (see also plots in Sect. 4). Figures 6 and 7 (Eureka) and Figs. 9 and 10

Fig. 6 Annual cycle of **a** wind speed at 3, ~8 (sonic anemometers), and 11 m (wind vane), **b** air temperature at 2, 6, and 10 m (RTD sensors), **c** soil temperature at 10, 20, 30, 45, 70, and 120 cm, and **d** soil heat flux (plates A and B) observed at Eureka in 2011. The data are based on 1-h averaging

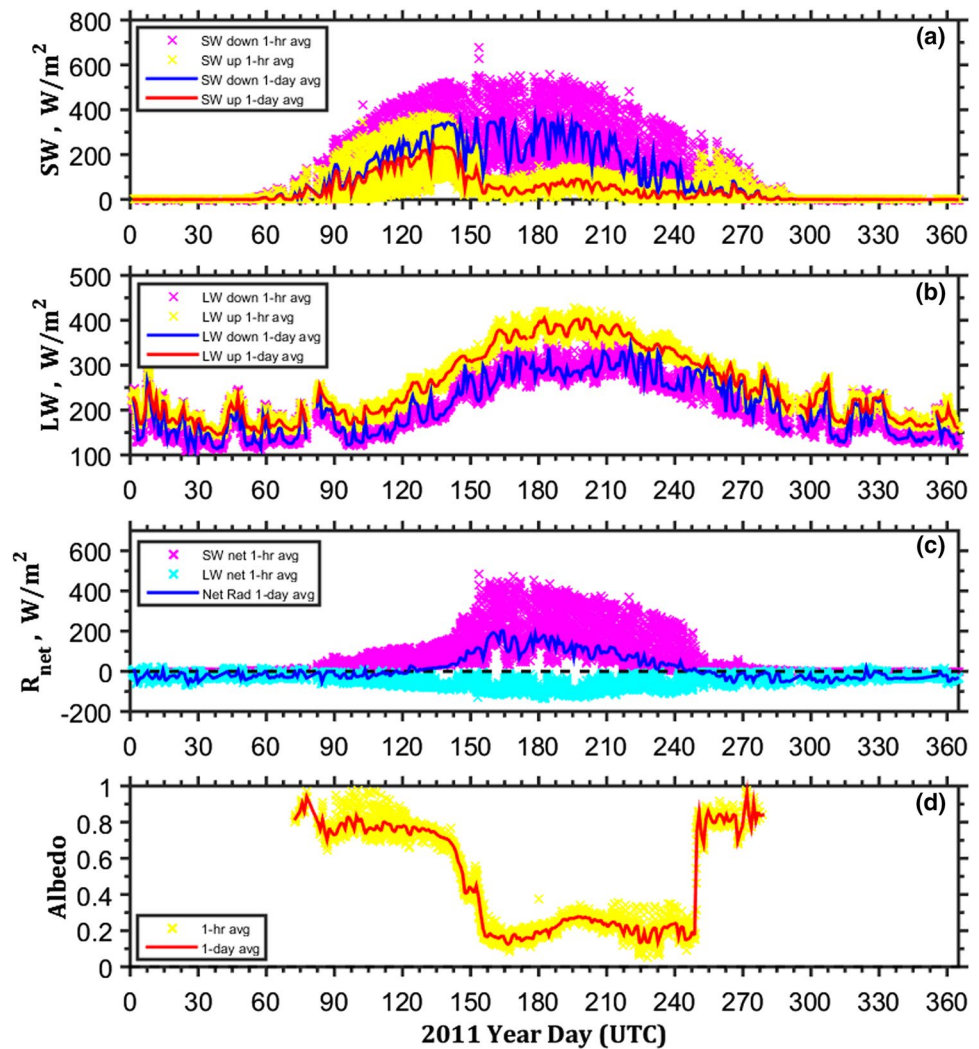


(Tiksi) show time series for 2011 and 2012, respectively, because these years have fewer data gaps compared to other years. Unlike ‘slow’ data, time series of post-processed turbulent fluxes are more intermittent (have more and longer data gaps) and have relatively large scatter in the measured values. Most loss of turbulence data are related to instrument malfunctions and the eddy-covariance quality filters described in Sect. 2. The winter period had much lower turbulence data retention due to the harsh conditions. The large scatter of the turbulent flux data is generally associated with the non-deterministic nature of turbulence. For this reason, Figs. 8a–c and 11a–c comprise the turbulent fluxes collected during several years that allow filling out gaps and reducing the scatter because the annual patterns of the fluxes for different years are very similar in a climatological sense. An annual cycle of turbulent fluxes calculated using eddy-covariance methodology collected at Eureka and Tiksi for a single year (2014) can be found in Uttal et al. (2016, their Fig. 7). Note that only direct eddy-covariance flux measurements are

used in Figs. 8a–c and 11a–c; that is, we have not filled missing turbulent flux data with semi-empirical bulk or gradients flux estimates derived from the ‘slow’ data.

Although Eureka and Tiksi are located on different continents and at different latitudes, the annual cycle of the surface meteorology (e.g., air and soil temperatures) and surface fluxes are qualitatively very similar (cf. Figs. 6, 7, 8, 9, 10, 11). The annual cycles of near-surface air temperature (SAT) display mid-winter (February) minima between -50 and -40 $^{\circ}\text{C}$ and mid-summer (July) maxima between $+15$ and $+25$ $^{\circ}\text{C}$ (Figs. 6b, c, 9b, c). Large variability of wintertime SAT are seen at both sites, with sudden magnitude changes of up to 20 $^{\circ}\text{C}$ noted. Variability of summertime SAT is larger at Tiksi than at Eureka. The SAT rises above freezing near June 1 at Eureka and slightly earlier at Tiksi, and falls below freezing at the two sites near September 1 and October 1, respectively. While the dates of the soil temperature minima and maxima are similar for the two sites, the amplitude of the annual cycle

Fig. 7 Annual cycle of **a** short-wave (SW) downwelling and upwelling radiation, **b** long-wave (LW) downwelling and upwelling radiation, **c** SW balance, LW balance, and net radiation, and **d** albedo (reflectivity of a surface) observed at Eureka in 2011. The data are based on 1-h (symbols) and 1-day (solid lines) averaging of 1-min radiation measurements made at the Flux Tower

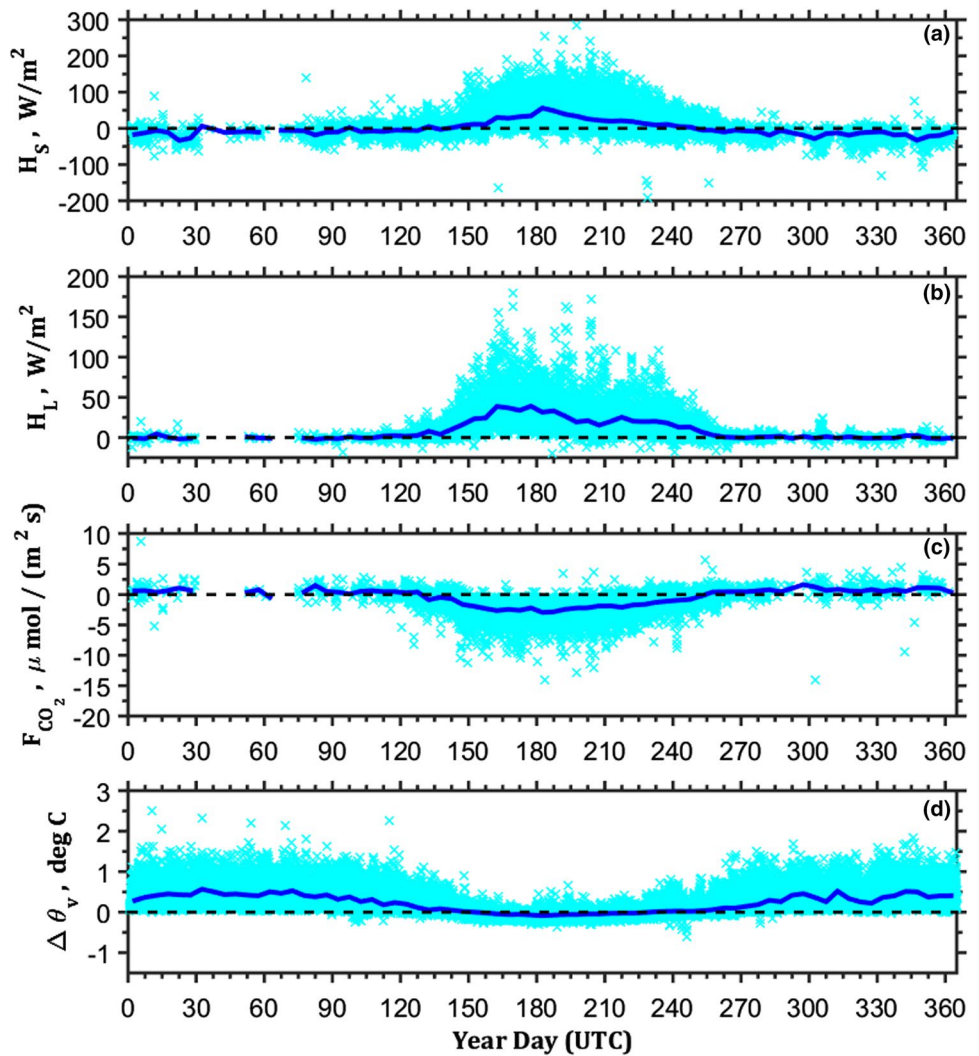


of soil temperature is significantly larger at Eureka than at Tiksi. The 10-cm soil temperature at Eureka varies from ~ -35 to -30 °C in February to from $+12$ to $+15$ °C in July, while at Tiksi it varies from ~ -22 to -18 °C in February to from $+1$ to $+4$ °C in July. The temperature gradient within the upper soil is larger at Eureka than at Tiksi, especially during summer. The soil conductive heat flux (Figs. 6d, 9d) is negative (upward heat flux or soil cooling) from early September to late March through early May at Eureka and from early-mid October to early April at Tiksi, with weak or slightly positive heat flux occurring during wintertime warming episodes. The magnitude of the wintertime negative heat flux is larger at Tiksi than at Eureka despite the warmer soil temperatures at Tiksi in late winter. While the magnitudes of the soil heating (positive soil heat flux) in summer are similar between the two sites, the diurnal variability is much greater at Eureka than at Tiksi. The brief warming event that occurred at Tiksi on May 5–7, 2012 [day of year (DOY) 126–128],

and impacted the soil thermal structure and soil conductive flux, does not occur every year.

The annual cycle of the downwelling SW radiation, SW_{down} , at hourly resolution shows daily maximum flux values in mid-summer of about 520 to 560 $W\ m^{-2}$ at Eureka (Fig. 7a) and much larger values of 700 – 760 $W\ m^{-2}$ at Tiksi (Fig. 10a), with SW_{down} beginning and ending about 30 days earlier and later, respectively, at Tiksi than at Eureka. These differences are consistent with the lower latitude of Tiksi. However, daily mean values of SW_{down} during mid-summer (blue line) are noticeably larger at Eureka than at Tiksi. This difference is due to greater “nighttime” insolation and less clouds at Eureka, and will be discussed later in this section. Downwelling longwave radiation, LW_{down} , reaches a minimum in late February and a maximum in July at both sites (Figs. 7b, 10b) in close correspondence with the temperature of the lower-troposphere. A net longwave radiation loss (difference between blue and red curves) occurs throughout the year at both sites. Hence, the net radiation, R_{net} , is weakly

Fig. 8 Seasonal cycles of turbulent fluxes (eddy-covariance) of **a** sensible heat at 3 and ~8 m, **b** latent heat (water vapor), **c** carbon dioxide, and **d** difference of air virtual potential temperature between 10 and 6 m levels observed at Eureka in 2009–2012, 2014 (year 2013 is missing). The data are based on 1-h (cyan x-symbols) and 5-day (blue solid lines) averaging of measurements made at the Eureka Flux Tower during the 5 years

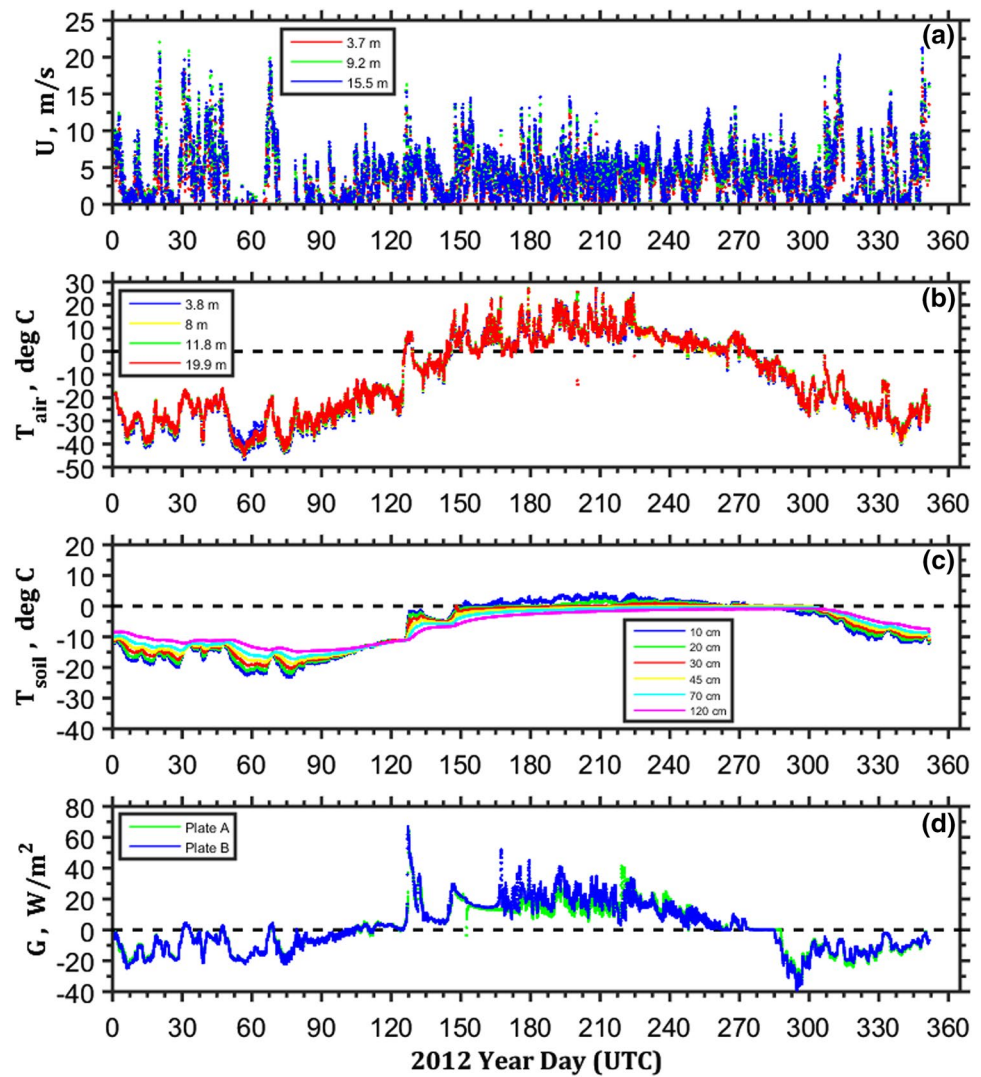


negative from September to May at Eureka and late-October to May at Tiksi (Figs. 7c, 10c). During summer at both sites, the peak in R_{net} occurs between early- and mid-June when the snow melts and the surface albedo reaches the low summertime values (Figs. 7c, d, 10c, d), and SW_{down} is near the annual peak. The net radiation decreases gradually and nearly linearly through the rest of the summer, primarily from the decrease in SW_{down} , becoming negative when the albedo increases suddenly with the first snowfall. Hence, the peak in R_{net} precedes the summer peak in SAT by about 1 month at both sites.

It has been long understood that the climatological annual cycle in SAT over land is largely controlled by solar forcing, and that observations of the annual cycle of air temperature could be approximated by a sinusoidal function (e.g., McKinnon et al. 2013 and references therein). At these high-latitude sites, the annual cycle in the envelope of daily maximum SW_{down} is only a partial sinusoid with a constant value ($= 0 \text{ W m}^{-2}$) for the remaining 3.5–5 months during

the polar night; the annual cycle of daily mean SW_{down} is a weaker match to a sinusoid, especially at Tiksi where summer clouds impact the fit. The annual cycle of SAT, as well as the soil temperature, does have a sinusoidal appearance during the time of the year when SW_{down} is significant, with a lag of about 30 days to the daily peak SW_{down} . During the remaining winter parts of the year, the SAT is approximately constant, though with large transitions likely related to cloud events and longwave radiative forcing (see below). The net surface radiative forcing (R_{net}) does not have a sinusoidal shape. It is nearly constant (weakly negative) for 8–9 months of the year, with a sudden peak in forcing in June followed by a near-linear summertime decline. Clearly, the annual cycle of the radiative forcing of the surface involves processes other than just the annual cycle of downwelling solar radiation; however, the SAT is surprisingly well correlated with the envelope of daily peak SW_{down} rather than with R_{net} . The air and soil temperatures, as well as ground flux, at each site are also highly correlated to one another on daily

Fig. 9 Annual cycle of **a** wind speed at 3.7, 9.2, 15.5 m (wind vanes), **b** air temperature at 3.8, 8, 11.8, 19.9 m (RTD sensors), **c** soil temperature at 10, 20, 30, 45, 70, and 120 cm, **d** soil heat flux (plates A and B) observed at Tiksi in 2012. The data are based on 1-h averaging

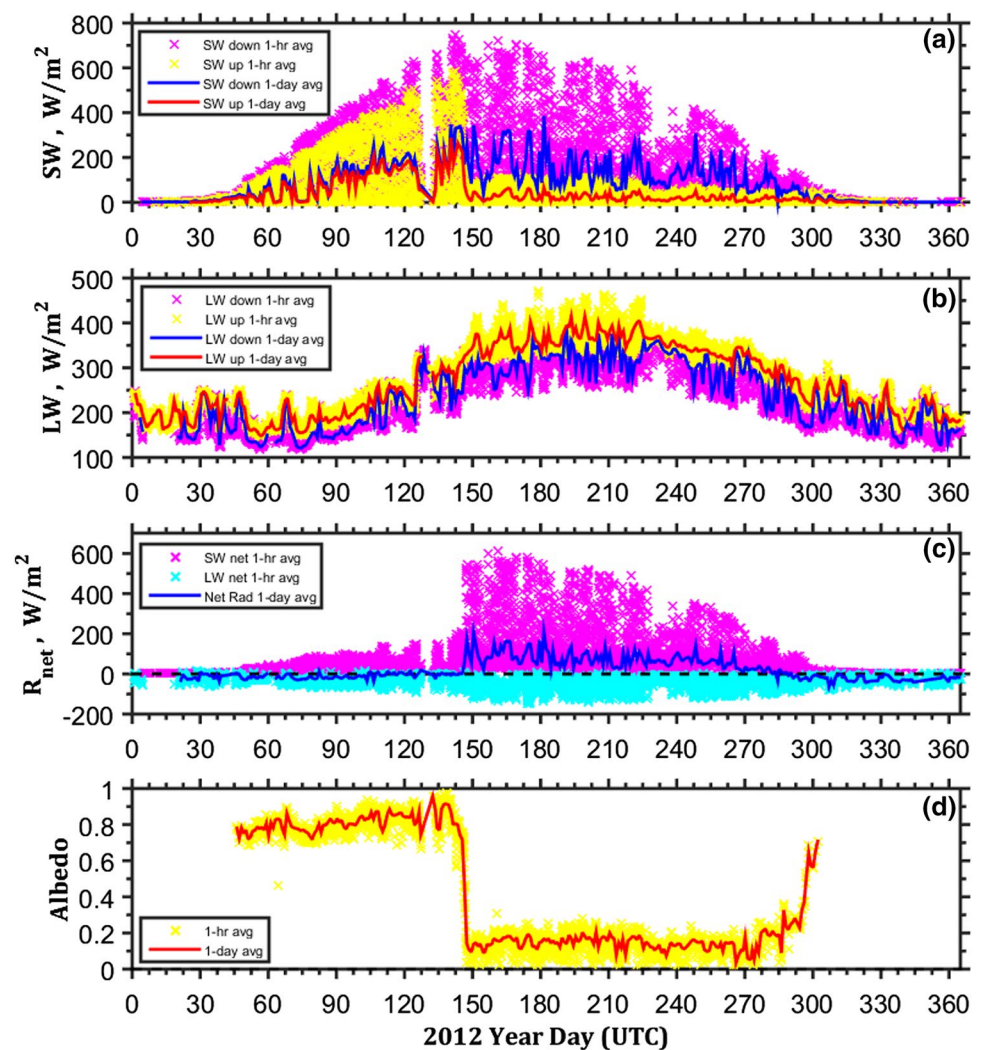


to weekly time scales. For instance, during the period of the year when the sun is above the horizon, diurnal variations of the air and soil temperatures associated with the diurnal cycles in SW_{down} are generally observed. The variations in the soil tend to be larger at Eureka than at Tiksi, while the SAT variations (and perhaps also wind speed variations) are larger at Tiksi (see Figs. 6, 9).

During the dark polar night, air and ground temperatures are strongly controlled by LW radiation generally associated with cloud cover (e.g., Stone 1997; Intrieri et al. 2002; Persson et al. 2002, 2016; Shupe and Intieri 2004). Figure 6b, c and 7b for Eureka and Fig. 9b, c and 10b for Tiksi show a strong correlation between LW_{down} and SAT, soil temperature, and soil heat flux. Clouds associated with synoptic or mesoscale atmospheric events and located within warmer air aloft produce significant increases in LW_{down} , forcing changes in the other near-surface parameters (e.g., Doyle et al. 2011). Increases in LW_{down} at Eureka may even at times be produced by snow blowing off nearby mountain peaks

(Lesins et al. 2012) and other low-level clouds (Mariani et al. 2012). LW radiation absorbed at the surface raises the snow skin temperature, enhancing LW upwelling radiation and reducing the upward conductive heat flux in the snowpack and soil below (Persson et al. 2016). Turbulent heat fluxes are also impacted by these events (Persson et al. 1999, 2016), as implied by the associated increases in SAT, though the recovery of covariance turbulence data during winter is too poor at Eureka and Tiksi to show this clearly. The perturbations in LW_{down} vary in intensity depending on cloud cover and opacity, but behave similarly in all cases. Increases in LW_{down} of $50 W m^{-2}$ are common, such as for a warm event at Eureka between approximately 9 and 19 February 2011 (DOY 40–50), but increases up to $100 W m^{-2}$ can occur if clouds are optically thick (Fig. 7b). For the 9–19 February Eureka case, the air temperature increased by $\approx 30 ^\circ C$ (Fig. 6b) and ground temperature at 10 cm depth increased by $\approx 12 ^\circ C$ (Fig. 6c). Often, such as for this event, the ground flux (Fig. 6d) and net longwave, $LW_{down} - LW_{up}$

Fig. 10 Annual cycle of **a** short-wave (SW) downwelling and upwelling radiation, **b** long-wave (LW) downwelling and upwelling radiation, **c** SW balance, LW balance, and net radiation, and **d** albedo (reflectivity of a surface) observed at Tiksi in 2012. The data are based on 1-h (symbols) and 1-day (solid lines) averaging of 1-min radiation measurements made at the BSRN tracker and albedo rack

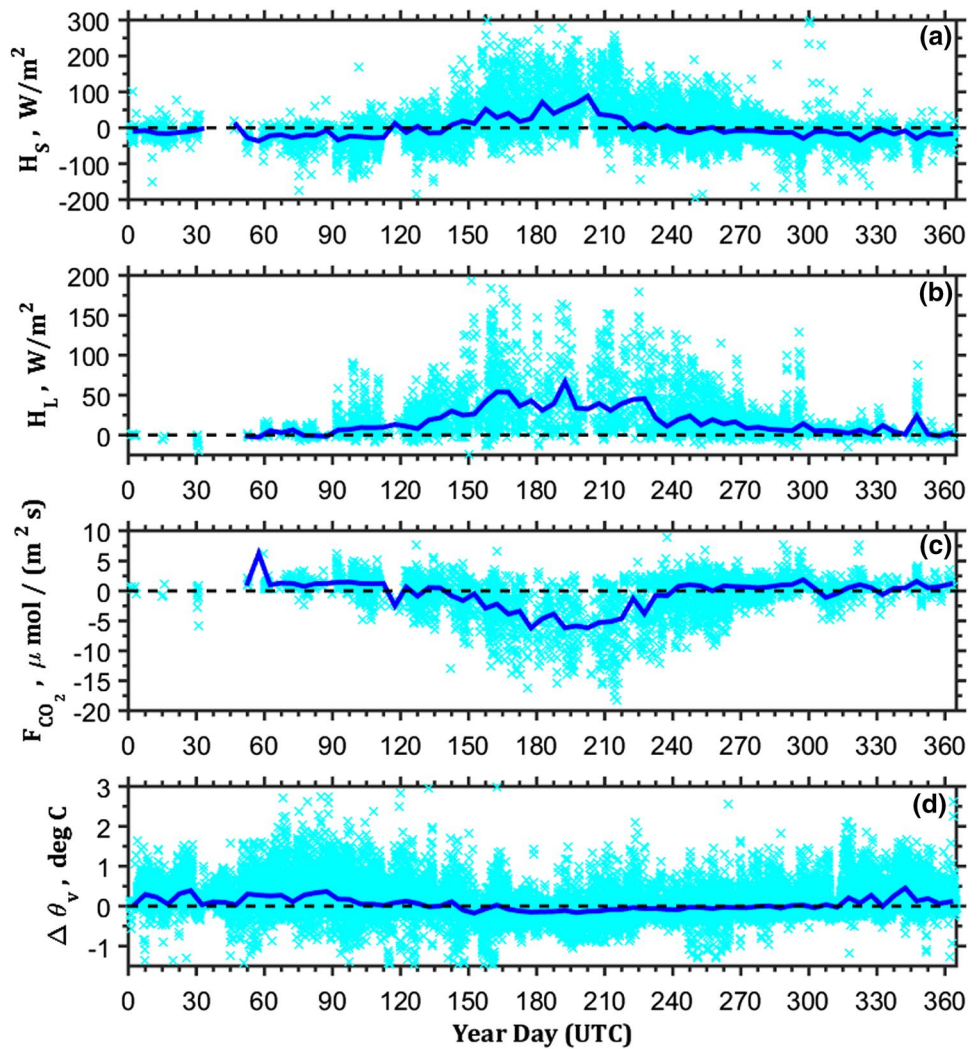


, (Fig. 7c) go to zero or become slightly positive, implying that these events can warm the permafrost even during winter. Such “warm” events associated with cloud radiative forcing and (likely) long-distance heat and moisture advection were common over the study period at both sites from autumn through spring; e.g., they were observed at Eureka during 2011 around DOY 84, 307 (Figs. 6, 7) and at Tiksi during 2012 around DOY 31, 47, 68, and 332 (Figs. 9, 10). While these radiatively-forced variations seem to dominate, ground temperature variability during winter can also be due to local thermal advection from nearby surface features with different energy balances, such as leads in coastal sea ice or land with thicker or thinner snow cover.

The seasonal patterns of the air temperature at the both sites (Figs. 6b, 9b) are highly correlated with soil thaw and freeze (Figs. 6c, 9c). Several dates are particularly notable in the annual time series plotted in Figs. 6, 7, 8, 9, 10 and 11. Frozen ground started warming when the surface heat flux crossed the zero-point around days 115–121 (25 April–1 May) at Eureka (Fig. 6d) and days 103–104 (12–13 April)

at Tiksi (Fig. 9d), and correspondingly, a change in the sign of the vertical gradient of subsurface temperature (Figs. 6c, 9c) was observed around days 120–122 (30 April–May 2) at Eureka (Fig. 6c) and days 103–105 (12–14 April) at Tiksi (Fig. 9c), consistent with the above zero-flux estimates. The timing of snow melt is evidenced by the large reduction in albedo that occurs on days 154–155 (3–4 June) in the vicinity of Eureka (Fig. 7d) and days 146–147 (May 26–27) in the vicinity of Tiksi (Fig. 10d) for the 2 years shown. Examination of other years show an inter-annual variability of ~5–10 days in the occurrence of the snow-free date, which is relatively small compared to variability in snow melt observed at Barrow, Alaska (of similar latitude to Tiksi) over the same time period (Cox et al. 2017). This snow-free date is determined radiometrically as the date when the surface albedo first drops below 30%, i.e., when the snow cover essentially disappears and is replaced by bare tundra (Stone et al. 2002). The last few days of snow melt are characterised by a rapid decrease in the upwelling (reflected) SW solar radiation (see Figs. 7a, 10a). As the ground becomes bare

Fig. 11 Seasonal cycles of turbulent fluxes (eddy-covariance) of **a** sensible heat at 3.5 and 9.5 m, **b** latent heat (water vapor), **c** carbon dioxide, and **d** difference of air virtual potential temperature between 9.8 and 5.8 m levels observed at Tiksi in 2012–2014. The data are based on 1-h (cyan x-symbols) and 5-day (blue solid lines) averaging of measurements made at the Tiksi Flux Tower during the 3 years



the uppermost layer of soil thaws, as occurs on days 154–157 (3–6 June) at Eureka (Fig. 6b, c) and on days 144–147 (23–26 May) at Tiksi (Fig. 9b, c). Finally, soils refreeze in the autumn on about days 247–250 (4–7 September) at Eureka (Fig. 6b, c) and on days 275–288 (1–14 October) at Tiksi (Fig. 9b, c). Long-term trends of some of these dates, such as the change in sign of the surface heat flux that occurs in spring or the dates of soil thaw and refreeze, can be used for monitoring Arctic climate change (e.g., Stone et al. 2002; Cox et al. 2017) and understand the physical processes and ecological responses associated with these changes. This is not done here, though, as the time series of these dates from this data set are currently too short to draw any conclusions regarding trends.

The larger amplitudes of the annual cycle of soil temperature and diurnal cycle of soil heat fluxes at Eureka were noted above. These differences are likely due to the much wetter soil and greater amounts of vegetation at Tiksi as compared to Eureka. This difference is visually illustrated by Fig. 4. Another marked difference between the two sites

is a well pronounced zero-curtain effect (e.g., Sumgin et al. 1940; Outcalt et al. 1990; Osterkamp and Romanovsky 1997; Barry and Gan 2011) observed in Tiksi in autumn on dates 275–296 (1–22 October) in the soil temperature time series (Fig. 9c, for 30 cm level) and on dates 275–287 in the ground heat flux records (Fig. 9d, for plate A). The autumn zero-curtain effect is associated with the phase transition of water to ice. As the summer active layer cools from the top, a freezing front propagates from the surface downward. Release of latent heat during the freezing of pore water results in the maintenance of isothermal temperatures at or just below 0 °C within the freezing active-layer over extended periods (Fig. 9c). The zero curtain decouples the permafrost from the atmosphere preventing cooling in the underlying ground layer (zero ground heat flux) for its duration (Fig. 9c), thereby protecting the ground from severe freezing. The lack of a pronounced zero-curtain effect at Eureka on dates 245–250 (Fig. 6c, d) is due to drier soils at this location, as discussed earlier. While there is no zero-curtain effect during spring thaw, the additional heat required to

melt the frozen soil moisture at Tiksi delays and suppresses the warming and downward growth of the summer active layer, producing a clear contrast in Tiksi summer soil temperatures and active-layer depth with those at Eureka, where most of the heat goes to warming the soil.

Note the apparent contradictory results for the summer thaw depth (also known as active layer or thaw line) and the topsoil temperature observed at Eureka and Tiksi (Figs. 6, 9). Specifically, the active layer is deeper and the topsoil temperature is higher at Eureka located about 9° north of the Tiksi observatory. The typical active layer thickness (ALT) is about 85 cm and the soil temperature is about 16 °C at 10 cm depth (≈ 18 °C at 5 cm depth) at the Eureka site (Fig. 6c) whereas the active layer is only ≈ 43 cm thick and the soil temperature is about 4 °C at 10 cm depth (≈ 7 °C at 5 cm depth) around the Tiksi flux tower (Fig. 9c). Similar ALT and the soil temperatures have been obtained at Eureka and Tiksi during other years (not shown). The different values of the ALT and soil temperature at these locations are perhaps due to the different regional environment as well as because of different latitudes (see a discussion in Sect. 4). Drier soils in Eureka are linked to thaw depth; that is, the surface soil moisture content (to a depth of 30 cm or so) decreases with increasing thaw depth (negative correlation). A thicker active layer increases the soil's water-holding capacity and surface water may drain away to deeper soil layers, leaving the topsoil dry (e.g., Yang et al. 2013). In turn, dry soils are generally heated more and faster than wet soils because water increases to heat capacity of the soil matrix.

Figures 8a–c and 11a–c show the seasonal cycles of the turbulent fluxes of the sensible heat, latent heat, and carbon dioxide at hourly and 5-day resolution observed in Eureka (during 2009–2012, 2014) and in Tiksi (during 2012–2014), respectively. The few wintertime turbulent flux data points that passed the QC algorithms suggest that all turbulent fluxes were small and mostly irregular during the polar night. In spring when solar radiation allows daytime heating of the surface, the turbulent fluxes start increasing, with a sudden increase near the time of the end of snow melt when the bare ground starts warming substantially. Maximum turbulent fluxes are reached in mid-June for latent heat fluxes, late June to mid-July for sensible heat fluxes, and July into early August for CO₂. This offset in the times of the peaks are likely due to the larger surface moisture just after snow melt enhancing the latent heat flux, greater surface heating from incoming radiation as opposed to drier surface conditions enhancing the sensible heat flux, and greater vegetation mass later in summer suppressing the CO₂ fluxes. On average, the turbulent CO₂ flux was mostly negative (uptake by the surface) during the short Arctic summer indicating that the Arctic tundra is a natural carbon sink during the growing season when surface is extensively covered with vegetation (see Figs. 3, 4). During late summer and early autumn all

turbulent fluxes rapidly decrease in magnitude, with daily mean fluxes of sensible heat and CO₂ reaching zero near the end of August at both sites and the daily-mean latent heat flux reaching zero 2–6 weeks later.

Figures 8d and 11d show the difference in virtual potential temperature between two atmospheric levels, $\Delta\theta_v$, based on 1-h (symbols) and 5-day (solid lines) averaging of measurements made at the Eureka and Tiksi flux towers, respectively. The difference in virtual potential temperature is positive when the atmospheric surface layer is stably stratified. The data show that the surface layer is generally unstable ($\Delta\theta_v < 0^\circ$) throughout the summer months, whereas during the winter cold season when the air temperature falls below freezing, surface radiative heat loss cools the atmosphere from below and the near-surface environment is generally stably stratified ($\Delta\theta_v > 0^\circ$). At Eureka, the surface layer is almost never neutral or unstable during polar winter, so the stable surface layer may last several months (see Fig. 8d) and the temperature inversions can be strong. While strong inversions can also occur in winter at Tiksi, episodes of unstable surface layers do occur so the stable surface layers may not be as long-lived as at Eureka.

4 Latitudinal variations in the surface fluxes and surface meteorology

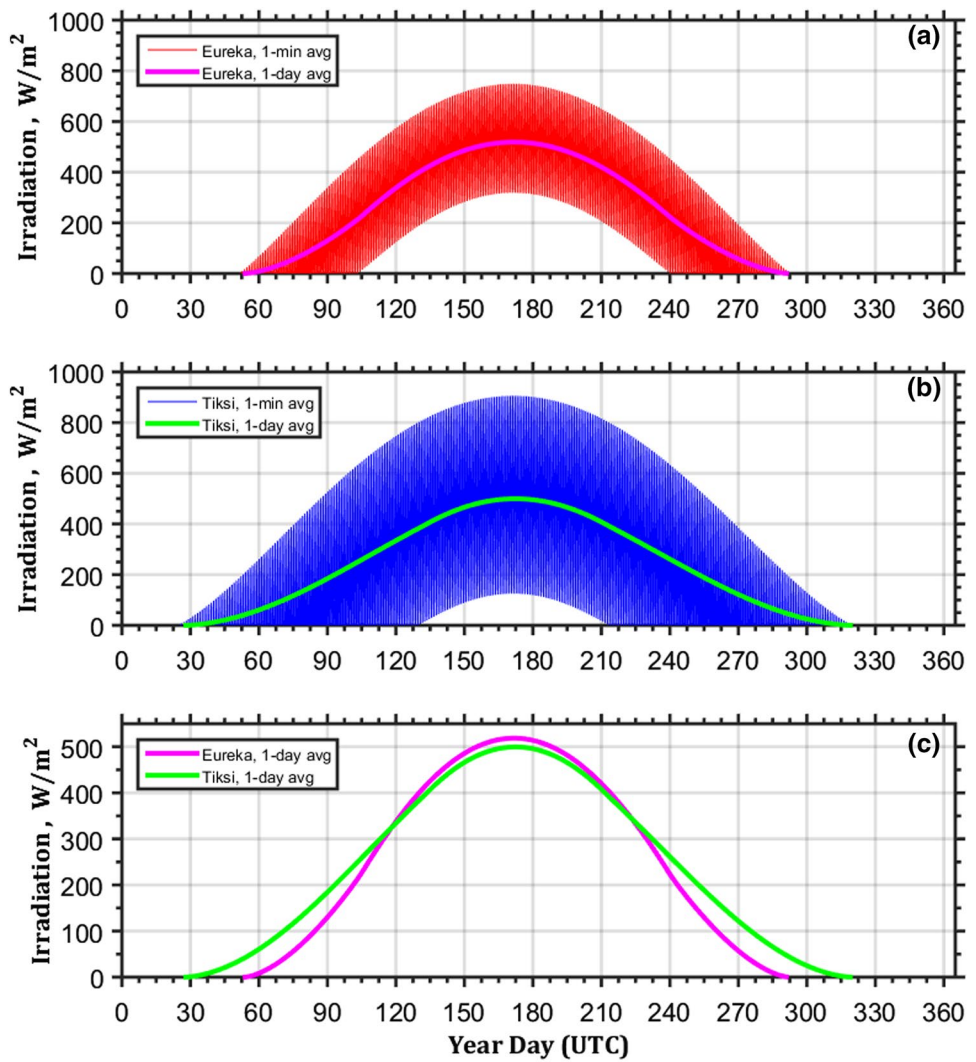
While Sect. 3 showed that the seasonal cycles of various meteorological parameters and fluxes at Eureka and Tiksi (Figs. 6, 7, 8, 9, 10, 11) are qualitatively similar, significant differences in a number of parameters between these sites were noted. These differences appear to be due to several factors, including differences in latitude, cloud characteristics, the annual cycle of snow cover, and soil type/moisture.

4.1 Solar radiation

The primary driver of latitudinal and seasonal variations in temperature and other parameters is the seasonally varying pattern of incident sunlight. Due to the fact that the solar radiation at the top of the atmosphere (TOA) is a function of latitude, time of year, and time of day (i.e., solar zenith angle), the higher latitudes generally receive less cumulative amount of net solar radiation over the entire year (annual mean) than lower latitudes. Thus, the length of the warm season (“Arctic summer”) is shorter at Eureka than at Tiksi as noted for our data above.

Figure 12 illustrates the above reasoning comparing daily variations and total daily amount of the TOA incident solar radiation (or insolation) over the entire year for Eureka (Fig. 12a) and Tiksi (Fig. 12b). Plots in Fig. 12 are based on solar ephemeris calculations described by Reda and Andreas (2003). At the peak of summer in Eureka, the sun revolves

Fig. 12 Annual cycle of the solar radiation at the ‘top’ of the atmosphere (TOA) at **a** Eureka (1-min and 1-day averaged), **b** Tiksi (1-min and 1-day averaged), and **c** Eureka and Tiksi (daily mean TOA flux). Plots are based on the algorithm by Reda and Andreas (2003)

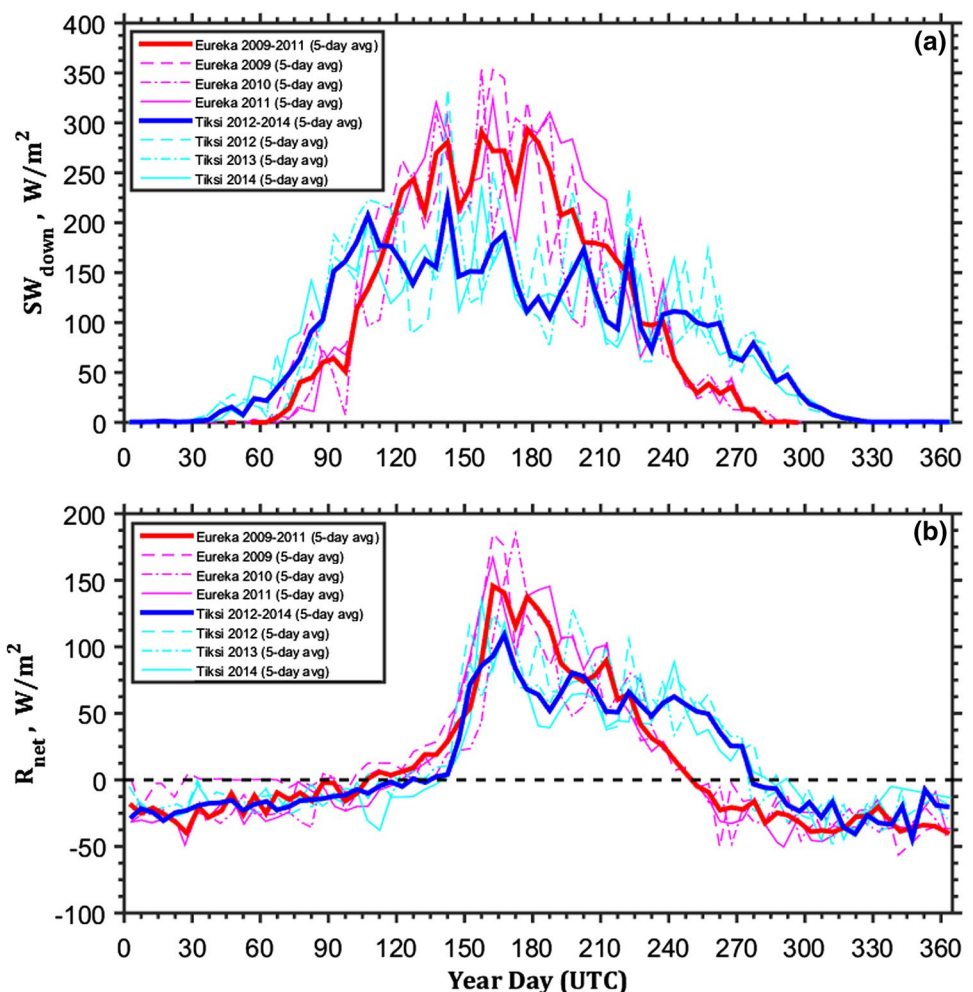


around the horizon, rising no higher than about 33° (42° in Tiksi) above the horizon at local noon, and dipping to about 14° (5° in Tiksi) above the horizon at local midnight. For this reason, the mid-summer amplitude (values near solar noon) in the incoming solar radiation is generally less at Eureka than at Tiksi (cf. Fig. 7a with 10a and 12a with 12b). Although the noon maximum of the downwelling SW radiation in summer is larger at Tiksi, the midnight minimum is larger at Eureka (cf. Fig. 12a, b). Consequently, the total daily amount of incoming solar radiation is larger at high-latitudes than at low-latitudes during the summer (e.g., Pidwirny 2006). For example, the daily mean TOA insolation at the North Pole on the summer solstice is about $522 W m^{-2}$, compared to a value of only $383 W m^{-2}$ at the equator (Serreze and Barry 2005). Thus, because of the combined effects of day length and solar zenith angle, Eureka receives more the incoming solar radiation at the TOA than Tiksi in the middle of Arctic summer between April 28 (DOY 118) and August 6 (DOY 218), while Tiksi receives more cumulative

amount of the incoming solar radiation over the entire year. Otherwise stated, the annual mean incoming solar radiation at the TOA is larger at Tiksi whereas the daily mean in summer is larger at Eureka (Fig. 12c). Hence, the latitudinal difference is the main reason that the envelope of the maximum mid-summer incoming surface solar radiation is generally less at Eureka than at Tiksi (cf. Fig. 7a with 10a and 12a with 12b). On the other hand, the greater nighttime solar elevation angle at Eureka is one reason that the daily mean solar radiation is greater at Eureka than at Tiksi (compare blue lines in Figs. 7a, 10a).

Figure 13 shows the annual cycle of the mean SW downwelling radiation (Fig. 13a) and the net radiation (Fig. 13b) measured at the surface at Eureka in 2009–2011 and Tiksi in 2012–2014 (only these years contain all four components of the solar radiation flux without long gaps). The data are based on 5-day averages of the 1-h averaged radiation measurements. These 3-year averages show that the surface at Eureka receives more incoming SW solar radiation than

Fig. 13 Annual cycle of **a** short-wave (SW) downwelling radiation and **b** net radiation observed at Eureka in 2009–2011 and Tiksi in 2012–2014. The net radiation is defined as the balance between downwelling (incoming) and upwelling (outgoing) SW and LW radiation. The data are based on 5-day averaging of 1-h radiation measurements



Tiksi between April 24 (DOY 114) and August 14 (DOY 226), roughly consistent with the period that the daily-mean TOA solar radiation is greater at Eureka. However, the insolation difference is between $40 W m^{-2}$ and $160 W m^{-2}$, which is 3–10 times as large as the $15 W m^{-2}$ expected from the latitudinal effect. Hence, the likely reason for the majority of the difference in incoming surface solar radiation between the two sites is a significant enhancement of solar attenuation by clouds at Tiksi compared to Eureka, likely due to a greater cloud fraction (cloud frequency) at Tiksi though also possibly impacted by differences in cloud optical depth.

According to Fig. 13b, the net surface radiation, R_{net} , is greater at Eureka for a brief period from late April through most of May and again from June 5 until August 6 (DOY 218), though only by 20 – $60 W m^{-2}$. This difference in R_{net} is primarily due to the difference in SW_{down} , though the lack of difference for a week or so near June 1 is likely due to the earlier date of bare ground (lower albedo and greater net SW radiation) at Tiksi. The reduction in the magnitude of the difference in R_{net} (Fig. 13b) compared to the difference in

SW_{down} (Fig. 13a) is likely due to the enhanced outgoing LW radiation (because of warmer surface temperature – compare Fig. 6b with 9b and Fig. 7b with 10b) and SW radiation (because of larger summer albedo – compare Figs. 7d, 10d) at Eureka compared to Tiksi.

4.2 Turbulent Fluxes and Atmospheric Stratification

Figures 8 and 11 show that the turbulent fluxes are consistent with the greater R_{net} values at solar noon at Tiksi than at Eureka (cf. Figs. 7c, 10c), as the former have daily maxima at Tiksi that are greater than those at Eureka. However, the 5-day averaged turbulent flux values are not very different from each other. According to Figs. 8 and 11, the summertime daily maximum sensible heat flux is about 150 – $200 W m^{-2}$ at Eureka (Fig. 8a) and about 200 – $250 W m^{-2}$ at Tiksi (Fig. 11a) and that for latent heat flux is about 100 – $150 W m^{-2}$ at Eureka (Fig. 8b) and about 150 – $175 W m^{-2}$ at Tiksi (Fig. 11b). For the both sites, typical values of the 5-day averaged turbulent fluxes in the summer season are 50 – $60 W m^{-2}$ for the sensible heat flux and 40 – $50 W m^{-2}$ for the latent

heat flux, although 5-day averaged values of the turbulent fluxes at Eureka are somewhat lower than at Tiksi.

Arctic locations with 24-h sunlight during summer months (Figs. 12, 13) can maintain a long-lived convective boundary layer (CBL) which, at lower latitudes, would be interrupted by stable nocturnal surface layers. Furthermore, high-latitude Arctic sites such as Eureka that have greater “nocturnal” insolation than other Arctic sites have even greater potential for maintaining such long-lived instability. Long-lived CBLs are associated with almost continuous unstable stratification, upward sensible heat flux, and downward carbon dioxide turbulent flux. A closer examination of the summertime vertical difference in virtual potential temperature, $\Delta\theta_v$, at Eureka (Fig. 8d) shows that the nocturnal stability generally becomes near neutral ($\Delta\theta_v \approx 0^\circ$) for a few hours and even sometimes stable ($\Delta\theta_v > 0^\circ$) every few nights. An examination of the hourly R_{net} values shows that the longwave cooling for a few nighttime hours is sufficient to compensate for shortwave heating for most of the summer, producing a near-zero or negative R_{net} value for a few hours each night. However, for the time period between 7 June and 8 July (DOY 158 – DOY 189), the LW_{net} loss at Eureka often does not completely compensate for the SW_{net} gain, and R_{net} is positive for all hours (minimum values of +15 to +30 W m^{-2}). This is the time period when long-lived CBLs ($\Delta\theta_v < 0^\circ$) are possible at Eureka and do primarily occur and can last for several weeks. Clouds on some nights, however, reduce the SW gain more than decrease the LW loss (negative cloud radiative forcing), resulting in negative R_{net} values even during this time period. Thus, there is a threshold of the net radiation below which the CBL cannot be maintained even within the Arctic Circle where it is 24 h of continuous daylight in summer. At Tiksi (Fig. 11d), the nocturnal stability in the summertime is greater and the number of consecutive nights with neutral or unstable stratification are fewer. Examination of the hourly R_{net} values at Tiksi shows that the LW loss is more than sufficient to compensate for the SW gain for some hours of most nights, even near the date of the summer solstice. Only on a few nights with no LW loss (due to clouds) is R_{net} positive, but then only marginally so (+10 to +20 W m^{-2}).

Note, that the long-lasting shallow CBLs are commonly observed over warm tropical oceans. The depth of the convective mixed layer (also referred to as the sub-cloud layer, a major part of the tropical marine atmospheric boundary layer) is quite variable, for example, ranging from 176 to 720 m (the mean is 539 m) over the western North Pacific (Geng et al. 2013).

During the dark Polar night, according to our data in Figs. 8d and 11d, the near-surface environment is generally stably stratified ($\Delta\theta_v > 0^\circ$). However, at Eureka, the surface layer is almost never neutral or unstable during winter, so long-lived stable boundary layers (SBL) can last several

months (Fig. 8d) and air/ground temperatures are strongly controlled by LW radiation associated generally with cloud cover. While strong inversions can also occur in winter at Tiksi, episodes of unstable surface layers do occur so the stable surface layers may not be as long-lived as at Eureka (Fig. 11d). However, the detailed discussion of the long-lived CBL and SBL is beyond the scope of this paper and will be considered separately from the main topic.

4.3 Active layer thickness (ALT) and topsoil temperature

The fact that Eureka receives more daily incoming solar radiation than Tiksi throughout the summer months leads to summer differences in the ABL structure (see Sect. 4.2), and can explain differences in the uppermost ground layer at these two Arctic stations. As discussed in Sect. 3, the active layer is deeper and the soil temperature is greater at Eureka than at Tiksi. Physically, it makes sense that this summertime difference is at least partly associated with the difference in incoming SW and net radiation at these locations before mid-August, as shown in Fig. 13. In other words, this difference is associated with latitudinal and cloud effects. Differences in soil moisture and soil type can also lead to similar differences in ALT and soil temperature, with the greater soil moisture at Tiksi leading to a greater soil heat capacity and hence a reduction in the warming produced by a given amount of heat. A quantitative analysis of the soil moisture at each site and the associated distribution of the net energy flux is necessary to fully understand the relative importance of the cloud/latitude effects or the soil moisture effect, but the necessary measurements are not currently available at these sites. Some other studies (see below) also generally confirm our findings that an average active layer (thaw) depth and topsoil temperature increases with increasing latitude in the range from around 70°N (Siberia and Alaska) to around 80°N (Canadian Archipelago and Svalbard).

Our estimates of the summer thaw depth in Tiksi (0.43 m) are close to the previous multi-year measurements of the ALT in this region. According to measurements by Watanabe et al. (2003, their Table 1) near Tiksi from 1997 to 2000, the averaged maximum thaw depth, which was observed at the end of August, was 0.4 ± 0.15 m (ranged from 1.2 to 0.2 m). Our measurements of the thaw depth in Tiksi are also consistent with the ALT ≈ 0.3 –0.5 m by Shiklomanov et al. (2010, their Fig. 7; Table 1) at Barrow, Alaska (71.3°N, 156.5°W) located at the same latitude as Tiksi. ALT measurements at the NOAA site in Barrow give the averaged thaw depth of 60 cm in 2013 and 2014 and 66 cm in 2015 (not shown) while average ALT measured across 20 sites on the Alaska North Slope from 1995 to 2014 was found to be 0.47 m (Romanovsky et al. 2014). Moreover, midsummer

topsoil temperatures ($\approx 3\text{--}5\text{ }^{\circ}\text{C}$ at 10 cm depth) observed in Tiksi (Fig. 6c) are consistent with similar measurements in Barrow (Shiklomanov et al. 2010, their Fig. 2) and Fish Creek, Alaska North Slope (Urban and Clow 2014, Fig. 6). Ground temperatures below the active layer in summer are reflective of longer term (annual and multi-annual time scales) conditions including previous year air temperature and previous winter snow cover (“memory effect”), e.g., Urban and Clow (2014).

The ALT (0.85 m) and the mid-summer topsoil temperature ($\approx 16\text{ }^{\circ}\text{C}$ at 10 cm depth) observed at Eureka is close to our estimates of the ALT ($\approx 0.8\text{--}0.9$ m) and the maximum soil temperature ($\approx 14\text{ }^{\circ}\text{C}$ at 10 cm depth) measured near the NOAA flux scaffolding and radiation mast at Alert (82.5°N, 62.3°W), located on Ellesmere Island in Canada about 400 km north of the Eureka observatory. The Alert data are available through the IASOA Data Portal (Starkweather and Uttal 2016) and the NSF Arctic Data Center mentioned in Sect. 2. Similar results were observed at Adventdalen, located 10 m above sea level in central Spitsbergen, Svalbard (78°N, 15°E) during 2000 and 2001. According to Oht (2003), the ALT in Adventdalen varied from 95 to 99 cm and the topsoil temperature was $\approx 17\text{ }^{\circ}\text{C}$.

These studies show differences in soil ALT and soil temperature similar to that noted at our two sites. However, the similar environments and limited number of sites used for these studies, the lack of cloud and detailed radiative data, and/or the lack of soil moisture and soil characterization in these studies make it difficult to discriminate and evaluate the relative impacts of latitude, clouds, snow cover, and soil characteristics on the summer ALT and soil temperature. Our study does have sufficient data to show that latitude and primarily clouds at least contribute to the differences in ALT and summer soil temperature between our two sites, though the lack of soil moisture data prevents us from making a quantitative assessment of the importance of soil moisture and soil type differences relative to the impacts of latitude and clouds. Furthermore, the spatial variability of the ABL processes may be strongly influenced by the complex topography. In several modelling and observation studies, for example Kilpeläinen et al. (2011), Kral et al. (2014) and references therein, was found that near-surface variables and turbulent surface fluxes had notable spatial variations due to the highly variable geography of Arctic fjords in Svalbard.

In this study we linked the total daily amount of the incoming solar radiation throughout the summer months with properties of the uppermost ground layer at the peak of summer observed at several Arctic sites. We argue that on average the active layer (thaw) is deeper and the topsoil temperature is higher at sites located around latitude 80°N (Canadian Archipelago and Svalbard) than at sites located around latitude 70°N (Siberia and Alaska). At first sight, this result contradicts to the traditional point view that the

ALT decreases with increasing latitude (e.g., Barry and Gan 2011). However, our findings are consistent with non-monotonic dependence of the ALT versus latitude, e.g., the ALT decreases with increasing latitude up to $\approx 70\text{--}75^{\circ}\text{N}$ (or so) and then the ALT begins to increase with further increasing latitude. The non-monotonic behavior of the ALT versus latitude is also supported by ALT estimates derived from satellite microwave remote sensing and ERA-Interim temperatures (Park et al. 2016, their Fig. 4). We have shown that latitude indeed contributes to this behavior in ALT and soil temperature, though we have also shown that cloud cover contributes more for Tiksi and Eureka. At Tiksi and Eureka, soil moisture undoubtedly also contributes but we don't have the data necessary to quantify its relative importance.

5 Summary and discussion

Multi-year measurements of surface fluxes (turbulent, radiative, and soil ground heat), surface meteorology, and basic surface/snow/permafrost parameters made at several near-coastal climate observatories located around the Arctic Ocean are used to investigate the annual cycle of the fluxes and its linkage to atmospheric and surface processes. In this multi-disciplinary synthesizing research, the data collected at Eureka (Canadian Arctic Archipelago) and Tiksi (Russia, East Siberia) located at two quite different latitudes (80.0°N and 71.6°N respectively) are analyzed in more detail. We compare annual cycles of the surface fluxes and other ancillary data to elucidate gross similarities expected of the pan-Arctic region but also significant regional differences in some seasonal cycles including spring onset of melt and autumn onset of freezing at the two Arctic stations. The differences can be attributed to both steep gradients in solar radiation as a function of latitude and local soil and local meteorological conditions forced by topography and mean long-range transports.

Although Eureka and Tiksi are located in different geographic zones, the annual course of the surface meteorology and the surface fluxes are qualitatively very similar. The air and soil temperatures display the familiar strong annual cycle with maximum of measured temperatures in midsummer and minimum during winter. The annual cycle of the turbulent fluxes is clearly evident with maximum flux magnitudes in mid-summer and fluxes that drop to small and mostly irregular values during the cold seasons when the ground is covered with snow, air temperatures are low, the surface layer is stable, and surface energy forcing is primarily through longwave radiation. Throughout the winter months, sensible heat flux on average is directed downward to the surface whereas both latent heat and carbon dioxide turbulent fluxes are upward. According to our data, during the polar night in the high Arctic regions, long-lived

stable boundary layers can last several months. During summer months, strong upward sensible and latent heat fluxes and downward carbon dioxide (uptake by the surface) are observed, indicating unstable (convective) stratification on average.

The primary driver of latitudinal and seasonal variations in temperature, surface fluxes, and other parameters is the seasonally varying pattern of incident sunlight, which is modulated by clouds. The solar radiation at the top of the atmosphere (TOA) is determined by well-known orbital parameters, including latitude and time of year. Noon TOA maximum of the downwelling SW radiation in summer is larger at Tiksi, but the midnight minimum is larger at Eureka. Because of the combined effects of day length and solar zenith angle, the TOA daily mean insolation at Eureka is greater than at Tiksi in the middle of Arctic summer. In other words, annual mean of the TOA incoming short-wave and net radiation is larger at Tiksi whereas a daily mean in summer is larger at Eureka for approximately a 3-month period. However, the difference in surface SW radiation between the two sites is 3–10 times greater than expected from the difference in TOA SW radiation, suggesting that clouds greatly enhance the SW radiation difference between the sites and that they are less frequent and perhaps less optically thick at Eureka than at Tiksi.

The differences in the variations of the incoming short-wave and net radiation lead to temporal and spatial differences in the structure of the atmospheric boundary layer and the temperature structure of the uppermost ground layer as follows:

- (i) The length of the warm season (“Arctic summer”), when average air temperatures are above freezing, is shorter at Eureka than at Tiksi because the higher latitudes generally receive the least cumulative amount of net solar radiation over the entire year (annual mean) than lower latitudes.
- (ii) The amplitude of hourly averaged surface fluxes near solar noon is generally less in Eureka than in Tiksi because the turbulent energy fluxes are highly correlated with the net radiation (e.g., Persson et al. 2016, Eq. 1). In Tiksi the sun rises higher in the sky at local noon in the summer than at Eureka and, therefore, the mid-summer amplitude (values near solar noon) in the incoming 1-h average solar radiation is generally less at Eureka than at Tiksi.
- (iii) In this study, we also linked the total daily amount of the incoming solar radiation throughout the summer months with the active layer thickness (ALT) and the topsoil temperature observed at the peak of summer. Our study shows that on average the active layer (or thaw line) is about twice as deep and topsoil temperatures in midsummer are about 10 °C

higher for the sites located at latitudes around 80°N (Canadian Archipelago and Svalbard) than at around 70°N (Alaska and Siberia). The latitudinal, cloud, and surface-characteristic effects on net radiation found at Eureka and Tiksi in summer months qualitatively explain the observed ALT and the topsoil temperatures at these sites.

- (iv) According to our observations, a convective boundary layer (CBL) in Eureka can reach long-lived quasi-stationary states for about one month centered on the summer solstice, though the observed maximum length was for 16 days in summer 2009 and typical lengths other years were 4–5 days. Such long-lived CBL are not observed at Tiksi, despite the fact that Tiksi is also located within the Arctic Circle where there is 24 h of continuous daylight in summer. This is because the “nighttime” summer insolation in Tiksi is generally not large enough to overcome the longwave radiative cooling. The longwave radiation provides the minimum threshold value for the net nighttime solar radiation needed to produce long-lived CBL in the Arctic.

Another marked difference between the two sites is a well pronounced zero-curtain effect observed in Tiksi at fall. The fall zero-curtain effect is associated with the phase transition of water to ice in wetter or/and water saturated soils. Soils in Eureka appear to be drier than in Tiksi. This fact can also explain the different behavior of the ground heat flux observed in Eureka and in Tiksi. We speculate in Sect. 3 that drier/wetter soils are linked to the thaw depth which, in turn, is mainly radiation driven.

It is plausible that the latitudinal gradient of the total daily amount of the incoming shortwave and net radiation during summer may contribute in part to Arctic (or polar) amplification in the summer period. For example, according to Lesins et al. (2012), the annually averaged surface temperature amplification factors exhibit a strong latitudinal dependence varying from 2.6 to 5.2 as the latitude increases from 50° to 80°N. Obviously, the latitudinal variations of the solar radiation should also lead to increase in the melt rate of sea ice with increasing latitude during summer.

Acknowledgements The US National Science Foundation’s Office of Polar Programs supported AAG, POGP, and RSS with award ARC 11-07428. AAG, APM, and IAR were supported by the US Civilian Research and Development Foundation (CRDF) with award RUG1-2976-ST-10. APM was also supported by the Russian Foundation for Basic Research with award RFBR 14-05-00677, the Ministry of Education and Science of the Russian Federation (Projects 2017-14-588-0005-003 and RFMEFI61617X0076), and the Roshydromet (Project CNTP 1.5.3.2). EAA, TU, CJC, and SMM received support from the National Oceanic and Atmospheric Administration (NOAA) Climate Program Office’s Arctic Research Program. We thank all the researchers who deploy, operate, and maintain the instruments at the

stations in frequently harsh Arctic conditions; their diligent and dedicated efforts are often underappreciated.

References

- Baldocchi D, Falge E, Gu L, Olson R, Hollinger D, Running S, Anthoni P, Bernhofer Ch, Davis K, Evans R, Fuentes J, Goldstein A, Katul G, Law B, Lee X, Malhi Y, Meyers T, Munger W, Oechel W, Paw UKT, Pilegaard K, Schmid HP, Valentini R, Verma S, Vesala T, Wilson K, Wofsy S (2001) FLUXNET: a new tool to study the temporal and spatial variability of ecosystem-scale carbon dioxide, water vapor, and energy flux densities. *Bull Am Meteorol Soc* 82(11):2415–2434
- Barry R, Gan TY (2011) *The global cryosphere: past, present and future*. Cambridge University Press, New York, p 472
- Blanchard Y, Royer A, O'Neill NT, Turner DD, Eloranta EW (2017) Thin ice clouds in the Arctic: cloud optical depth and particle size retrieved from ground-based thermal infrared radiometry. *Atmos Meas Tech* 10(6):2129–2147. <https://doi.org/10.5194/amt-10-2129-2017>
- Brooks IM, Tjernström M, Persson POG, Shupe MD, Atkinson RA, Canut G, Birch CE, Mauritsen T, Sedlar J, Brooks BJ (2017) The turbulent structure of the Arctic summer boundary layer during ASCOS. *J Geophys Res Atmos* 122:9685–9704. <https://doi.org/10.1002/2017JD027234>
- Cox CJ, Walden VP, Rowe PM (2012) A comparison of the atmospheric conditions at Eureka, Canada, and Barrow, Alaska (2006–2008). *J Geophys Res* 117(D12):D12204. <https://doi.org/10.1029/2011JD017164>
- Cox CJ, Turner DD, Rowe PM, Shupe MD, Walden VP (2014) Cloud microphysical properties retrieved from downwelling infrared radiance measurements made at Eureka, Nunavut, Canada (2006–2009). *J Appl Meteorol Climatol* 53(3):772–791. <https://doi.org/10.1175/JAMC-D-13-0113.1>
- Cox CJ, Walden VP, Rowe PM, Shupe MD (2015) Humidity trends imply increased sensitivity to clouds in a warming Arctic. *Nat Commun* 6:10117. <https://doi.org/10.1038/ncomms10117>
- Cox CJ, Stone RS, Douglas DC, Stanitski DM, Divoky GJ, Dutton GS, Sweeney C, George JC, Longenecker DU (2017) Drivers and environmental responses to the changing annual snow cycle of northern Alaska. *Bull Am Meteorol Soc*. <https://doi.org/10.1175/BAMS-D-16-0201.1> (in press)
- Crawford A, Serreze M (2015) A new look at the summer Arctic frontal zone. *J Clim* 28(2):737–754. <https://doi.org/10.1175/JCLI-D-14-00447.1>
- de Boer G, Tripoli GJ, Eloranta EW (2008) Preliminary comparison of CloudSAT-derived microphysical quantities with ground-based measurements for mixed-phase stratus. *J Geophys Res* 113(D8):D00A06. <https://doi.org/10.1029/2008JD010029>
- de Boer G, Eloranta EW, Shupe MD (2009) Arctic mixed-phase stratus properties from multiple years of surface-based measurements at two high-latitude locations. *J Atmos Sci* 66(9):2874–2887. <https://doi.org/10.1175/2009JAS3029.1>
- Doyle JG, Lesins G, Thakray CP, Perro C, Nott GJ, Duck TJ, Damoah R, Drummond JR (2011) Water vapor intrusions into the High Arctic during winter. *Geophys Res Lett* 38(12):L12806. <https://doi.org/10.1029/2011GL047493>
- Fast H, Mittermeier RL, Makino Y (2011) A ten-year record of Arctic trace gas total column measurements at Eureka, Canada, from 1997 to 2006. *Atmos Ocean* 49(2):67–94. <https://doi.org/10.1080/07055900.2011.562470>
- Francis JA, Hunter E, Key J, Wang X (2005) Clues to variability in Arctic minimum sea ice extent. *Geophys Res Lett* 32(21):L21501. <https://doi.org/10.1029/2005GL024376>
- Garratt JR (1992) *The atmospheric boundary layer*. Cambridge University Press, UK, p 316
- Geng B, Yoneyama K, Shirooka R (2013) Thermodynamic structure and evolution of the atmospheric mixed layer over the western North Pacific during the summer monsoon onset. *J Geophys Res Atmos* 118(11):5655–5666. <https://doi.org/10.1002/jgrd.50242>
- Gold AU, Kirk K, Morrison D, Lynds S, Buhr Sullivan S, Grachev A, Persson O (2015) Arctic climate connections curriculum: a model for bringing authentic data into the classroom. *J Geosci Educ* 63(3):185–197. <https://doi.org/10.5408/14-030.1>
- Grachev AA, Fairall CW, Persson POG, Andreas EL, Guest PS (2005) Stable boundary-layer scaling regimes: the SHEBA data. *Bound Layer Meteorol* 116(2):201–235. <https://doi.org/10.1007/s10546-004-2729-0>
- Grachev AA, Bariteau L, Fairall CW, Hare JE, Helmig D, Hueber J, Lang EK (2011) Turbulent fluxes and transfer of trace gases from ship-based measurements during TexAQS 2006. *J Geophys Res* 116(D13):D13110. <https://doi.org/10.1029/2010JD015502>
- Grachev AA, Andreas EL, Fairall CW, Guest PS, Persson POG (2013) The critical Richardson number and limits of applicability of local similarity theory in the stable boundary layer. *Bound Layer Meteorol* 147(1):51–82. <https://doi.org/10.1007/s10546-012-9771-0>
- Grachev AA, Andreas EL, Fairall CW, Guest PS, Persson POG (2015) Similarity theory based on the Dougherty–Ozmidov length scale. *Q J R Meteorol Soc*. <https://doi.org/10.1002/qj.2488>
- Grachev AA, Leo LS, Di Sabatino S, Fernando HJS, Pardyjak ER, Fairall CW (2016) Structure of turbulence in katabatic flows below and above the wind-speed maximum. *Bound Layer Meteorol* 159(3):469–494. <https://doi.org/10.1007/s10546-015-0034-8>
- Halliwel DH, Rouse WR (1987) Soil heat flux in permafrost: characteristics and accuracy of measurement. *J Climatol* 7(6):571–584. <https://doi.org/10.1002/joc.3370070605>
- Harazono Y, Mano M, Miyata A, Zulueta RC, Oechel WC (2003) Inter-annual carbon dioxide uptake of a wet sedge tundra ecosystem in the Arctic. *Tellus* 55B(2):215–231. <https://doi.org/10.1034/j.1600-0889.2003.00012.x>
- Intrieri JM, Fairall CW, Shupe MD, Persson POG, Andreas EL, Guest PS, Moritz RE (2002) An annual cycle of Arctic surface cloud forcing at SHEBA. *J Geophys Res* 107(C10):8039. <https://doi.org/10.1029/2000JC000439>
- Ishii S, Shibata T, Nagai T, Mizutani K, Itabe T, Hirota M, Fujimoto T, Uchino O (1999) Arctic haze and clouds observed by lidar during four winter seasons of 1993–1997 at Eureka, Canada. *Atmos Environ* 33(16):2459–2470. [https://doi.org/10.1016/S1352-2310\(98\)00397-5](https://doi.org/10.1016/S1352-2310(98)00397-5)
- Ivanov NE, Makshtas AP (2012) Long-term variability of climate characteristics in the Northern Yakutia. *Probl Arctic Antarct* 4(94):5–22 (in Russian)
- Ivanov NE, Makshtas AP, Shutilin SV, Gun RM (2009a) Long-term variability of climate characteristics in the area of Tiksi hydrometeorological observatory. *Probl Arctic Antarct* 1(81):24–41 (in Russian)
- Ivanov NE, Makshtas AP, Shutilin SV (2009b) Long-term variability of climate characteristics in the area of Tiksi hydrometeorological observatory. Part 2. Seasonal variability. *Probl Arctic Antarct* 3(83):93–113 (in Russian)
- Kaimal JC, Finnigan JJ (1994) *Atmospheric boundary layer flows: their structure and measurements*. Oxford University Press, New York, p 289
- Kaufman DS, Schneider DP, McKay NP, Ammann CM, Bradley RS, Briffa KR, Miller GH, Otto-Bliesner BL, Overpeck JT, Vinther BM, Arctic Lakes 2K Project Members (2009) Recent warming reverses long-term Arctic cooling. *Science* 325(5945):1236–1239. <https://doi.org/10.1126/science.1173983>
- Kilpeläinen T, Vihma T, Ólafsson H (2011) Modeling of spatial variability and topographic effects over

- Arctic fjords in Svalbard. *Tellus A* 63(2):223–237. <https://doi.org/10.1111/j.1600-0870.2010.00481.x>
- Kral ST, Sjöblom A, Nygård T (2014) Observations of summer turbulent surface fluxes in a high Arctic fjord. *Q J R Meteorol Soc* 140(679B):666–675. <https://doi.org/10.1002/qj.2167>
- Kug J-S, Jeong J-H, Jang Y-S, Kim B-M, Folland CK, Min S-K, Son S-W (2015) Two distinct influences of Arctic warming on cold winters over North America and East Asia. *Nat Geosci* 8:759–762. <https://doi.org/10.1038/ngeo2517>
- Kwon H-J, Oechel WC, Zulueta RC, Hastings SJ (2006) Effects of climate variability on carbon sequestration among adjacent wet sedge tundra and moist tussock tundra ecosystems. *J Geophys Res* 111(G3):G03014. <https://doi.org/10.1029/2005JG000036>
- Laurila T, Soegaard H, Lloyd CR, Aurela M, Tuovinen J-P, Nordstroem C (2001) Seasonal variations of net CO₂ exchange in European Arctic ecosystems. *Theor Appl Climatol* 70(1–4):183–201. <https://doi.org/10.1007/s007040170014>
- Laxon S, Peacock N, Smith D (2003) High interannual variability of sea ice thickness in the Arctic region. *Nature* 425(6961):947–950. <https://doi.org/10.1038/nature02050>
- Lesins G, Bourdages L, Duck TJ, Drummond JR, Eloranta EW, Walden VP (2009) Large surface radiative forcing from topographic blowing snow residuals measured in the High Arctic at Eureka. *Atmos Chem Phys* 9(6):1847–1862. <https://doi.org/10.5194/acp-9-1847-2009>
- Lesins G, Duck TJ, Drummond JR (2010) Climate trends at Eureka in the Canadian high Arctic. *Atmos Ocean* 48(2):59–80. <https://doi.org/10.3137/AO1103.2010>
- Lesins G, Duck TJ, Drummond JR (2012) Surface energy balance framework for Arctic amplification of climate change. *J Clim* 25(23):8277–8288. <https://doi.org/10.1175/JCLI-D-11-00711.1>
- Mariani Z, Strong K, Wolff M, Rowe P, Walden V, Fogal PF, Duck T, Lesins G, Turner DS, Cox C, Eloranta E, Drummond JR, Roy C, Turner DD, Hudak D, Lindenmaier IA (2012) Infrared measurements in the Arctic using two atmospheric emitted radiance interferometers. *Atmos Meas Tech* 5(2):329–344. <https://doi.org/10.5194/amt-5-329-2012>
- Matsui N, Long CN, Augustine J, Halliwell D, Uttal T, Longenecker D, Niebergall O, Wendell J, Albee R (2012) Evaluation of Arctic broadband surface radiation measurements. *Atmos Meas Tech* 5(2):429–438. <https://doi.org/10.5194/amt-5-429-2012>
- Mbufong HN, Lund M, Aurela M, Christensen TR, Eugster W, Friberg T, Hansen BU, Humphreys ER, Jackowicz-Korczynski M, Kutzbach L, Lafleur PM, Oechel WC, Parmentier FJW, Rasse DP, Rocha AV, Sachs T, van der Molen MK, Tamstorf MP (2014) Assessing the spatial variability in peak season CO₂ exchange characteristics across the Arctic tundra using a light response curve parameterization. *Biogeosciences* 11(17):4897–4912. <https://doi.org/10.5194/bg-11-4897-2014>
- McBean G, Alekseev G, Chen D, Forland E, Fyfe J, Groisman PY, King R, Melling H, Vose R, Whitfield PH (2005) Arctic climate: past and present. In: Symon C, Arris L, Heal B (eds) Arctic climate impact assessment, ACIA. Cambridge University Press, Cambridge, 21–60
- McKinnon KA, Stine AR, Huybers P (2013) The spatial structure of the annual cycle in surface temperature: amplitude, phase, and lagrangian history. *J Clim* 26(20):7852–7862. <https://doi.org/10.1175/JCLI-D-13-00021.1>
- Nakai T, Iwata H, Harazono Y (2011) Importance of mixing ratio for a long-term CO₂ flux measurement with a closed-path system. *Tellus* 63B(3):302–308. <https://doi.org/10.1111/j.1600-0889.2011.00538.x>
- Oechel WC, Vourlitis GL, Hastings SJ, Zulueta RC, Hinzman L, Kane D (2000) Acclimation of ecosystem CO₂ exchange in the Alaskan Arctic in response to decadal climate warming. *Nature* 406(6799):978–981. <https://doi.org/10.1038/35023137>
- Oechel WC, Laskowski CA, Burba G, Gioli B, Kalhori AAM (2014) Annual patterns and budget of CO₂ flux in an Arctic tussock tundra ecosystem. *J Geophys Res Biogeosci* 119(3):323–339. <https://doi.org/10.1002/2013JG002431>
- Oht M (2003) Impact of meteorological factors on active layer development in central Spitsbergen. In: Phillips M, Springman SM, Aronson LU (eds) Permafrost, Proceedings of the eighth international conference on permafrost, 21–25 July 2003, Zurich, Switzerland, Swets & Zeitlinger, Lisse, pp 845–850. http://www.arlis.org/docs/vol11/ICOP/55700698/Pdf/Chapter_148.pdf
- Osterkamp TE, Romanovsky VE (1997) Freezing of the active layer on the coastal plain of the Alaskan Arctic. *Permafrost Periglacial Process* 8(1):23–44
- Outcalt SI, Nelson FE, Hinkel KM (1990) The zero-curtain effect: heat and mass transfer across an isothermal region in freezing soil. *Water Resour Res* 26(7):1509–1516. <https://doi.org/10.1029/WR026i007p01509>
- Overland JE, Wang M, Salo S (2008) The recent Arctic warm period. *Tellus* 60A(4):589–597. <https://doi.org/10.1111/j.1600-0870.2008.00327.x>
- Overland JE, Wood KR, Wang M (2011) Warm Arctic-cold continents: impacts of the newly open Arctic Sea. *Polar Res* 30:15787. <https://doi.org/10.3402/polar.v30i0.15787>
- Park H, Kim Y, Kimball JS (2016) Widespread permafrost vulnerability and soil active layer increases over the high northern latitudes inferred from satellite remote sensing and process model assessments. *Remote Sens Environ* 175:349–358. <https://doi.org/10.1016/j.rse.2015.12.046>
- Persson POG (2012) Onset and end of the summer melt season over sea ice: thermal structure and surface energy perspective from SHEBA. *Clim Dyn* 39(6):1349–1371. <https://doi.org/10.1007/s00382-011-1196-9>
- Persson POG, Uttal T, Intrieri JM, Fairall CW, Andreas EL, Guest PS (1999) Observations of large thermal transitions during the Arctic night from a suite of sensors at SHEBA. American Meteorological Society, 79th Annual Meeting, 3rd Symposium on Integrated Observing Systems, 10–15 January 1999, Dallas TX, Symposium Preprints, pp 171–174, Paper J5.3
- Persson POG, Fairall CW, Andreas EL, Guest PS, Perovich DK (2002) Measurements near the atmospheric surface flux group tower at SHEBA: near-surface conditions and surface energy budget. *J Geophys Res* 107(C10):8045. <https://doi.org/10.1029/2000JC000705>
- Persson POG, Shupe M, Perovich D, Solomon A (2016) Linking atmospheric synoptic transport, cloud phase, surface energy fluxes, and sea-ice growth: observations of midwinter SHEBA conditions. *Clim Dyn*. <https://doi.org/10.1007/s00382-016-3383-1>
- Pidwirny M (2006) Earth–sun relationships and insolation. In: Fundamentals of physical geography, 2nd edn. <http://www.physicalgeography.net/fundamentals/6i.html>
- Polyakov IV, Walsh JE, Kwok R (2012) Recent changes of Arctic multiyear sea ice coverage and the likely causes. *Bull Am Meteorol Soc* 93(2):145–151. <https://doi.org/10.1175/BAMS-D-11-00070.1>
- Reda I, Andreas A (2003) Solar position algorithm for solar radiation applications. *NREL Report No. TP-560-34302*, Revised January 2008, 55 p. <http://www.nrel.gov/docs/fy08osti/34302.pdf>
- Romanovsky VE, Sazonova TS, Balobaev VT, Shender NI, Sergueev DO (2007) Past and recent changes in air and permafrost temperatures in eastern Siberia. *Glob Planet Change* 56(3–4):399–413. <https://doi.org/10.1016/j.gloplacha.2006.07.022>
- Romanovsky VE, Cable WG, Kholodov SS, Marchenko SS, Panda SK, Shiklomanov NI, Walker DA (2014) Changes in permafrost and active-layer thickness due to climate in the Prudhoe Bay region and North Slope, AK. Arctic Change 2014, Ottawa, Canada, Dec. 8–12. http://www.geobotany.uaf.edu/library/posters/Romanovsky2014_OttawaAC2014_pos20141205.pdf

- Romanovsky VE, Smith SL, Isaksen K, Shiklomanov NI, Streletskiy DA, Kholodov AL, Christiansen HH, Drozdov DS, Malkova GV, Marchenko SS (2016) Terrestrial permafrost [in “State of the Climate in 2015”]. *Bull Am Meteorol Soc* 97(8):S149–S152
- Schotanus P, Nieuwstadt FTM, De Bruin HAR (1983) Temperature measurement with a sonic anemometer and its application to heat and moisture fluxes. *Bound Layer Meteorol* 26(1):81–93. <https://doi.org/10.1007/BF00164332>
- Serreze MC, Barry RG (2005) *The Arctic climate system*. Cambridge University Press, Cambridge, p 385
- Serreze MC, Holland MM, Stroeve J (2007) Perspectives on the Arctic's shrinking sea-ice cover. *Science* 315:1533–1536. <https://doi.org/10.1126/science.1139426>
- Shiklomanov NI, Streletskiy DA, Nelson FE, Hollister RD, Romanovsky VE, Tweedie CE, Bockheim JG, Brown J (2010) Decadal variations of active-layer thickness in moisture-controlled landscapes, Barrow, Alaska. *J Geophys Res* 115(G4):G00I04. <https://doi.org/10.1029/2009JG001248>
- Shupe MD (2011) Clouds at Arctic atmospheric observatories, Part II: thermodynamic phase characteristics. *J Appl Meteorol Climatol* 50(3):645–661. <https://doi.org/10.1175/2010JAMC2468.1>
- Shupe MD, Intrieri JM (2004) Cloud radiative forcing of the Arctic surface: the influence of cloud properties, surface albedo, and solar zenith angle. *J Clim* 17(3):616–628
- Shupe MD, Walden VP, Eloranta E, Uttal T, Campbell JR, Starkweather SM, Shiobara M (2011) Clouds at Arctic atmospheric observatories, Part I: occurrence and macrophysical properties. *J Appl Meteorol Climatol* 50(3):626–644. <https://doi.org/10.1175/2010JAMC2467.1>
- Starkweather S, Uttal T (2016) Cyberinfrastructure and laboratory support for the integration of Arctic atmospheric research. *Bull Am Meteorol Soc* 97(6):917–922. <https://doi.org/10.1175/BAMS-D-14-00144.1>
- Stone RS (1997) Variations in western Arctic temperatures in response to cloud radiative and synoptic-scale influences. *J Geophys Res* 102(D18):21,769–21,776. <https://doi.org/10.1029/97JD01840>
- Stone RS, Dutton EG, Harris JM, Longenecker D (2002) Earlier spring snowmelt in northern Alaska as an indicator of climate change. *J Geophys Res* 107(D10):4089. <https://doi.org/10.1029/2000JD000286>
- Stroeve J, Holland MM, Meier W, Scambos T, Serreze M (2007) Arctic sea ice decline: faster than forecast. *Geophys Res Lett* 34(9):L09501. <https://doi.org/10.1029/2007GL029703>
- Sumgin MI, Kachurin SP, Tolstikhin NI, Tumel' VF (1940) *General geocryology* (in Russian). Academy of Science of the USSR, Moscow, p 240
- Sun L, Perlwitz J, Hoerling M (2016) What caused the recent “Warm Arctic, Cold Continents” trend pattern in winter temperatures? *Geophys Res Lett* 43(10):5345–5352. <https://doi.org/10.1002/2016GL069024>
- Urban FE, Clow GD (2014) DOI/GTN-P climate and active-layer data acquired in the national petroleum reserve—Alaska and the Arctic National Wildlife Refuge, 1998–2013. US Geological Survey Data Series, 812. <https://doi.org/10.3133/ds812>
- Uttal T, Makhtas A, Laurila T (2013) The Tiksi International hydro-meteorological observatory—an Arctic members partnership. *WMO Bull* 62(1):22–26
- Uttal T, Starkweather S, Drummond JR, Vihma T, Makhtas AP, Darby LS, Burkhart JF, Cox CJ, Schmeisser LN, Haiden T, Maturilli M, Shupe MD, de Boer G, Saha A, Grachev AA, Crepinsek SM, Bruhwiler L, Goodison B, McArthur B, Walden VP, Dlugokencky EJ, Persson POG, Lesins G, Laurila T, Ogren JA, Stone R, Long CN, Sharma S, Massling A, Turner DD, Stanitski DM, Asmi E, Aurela M, Skov H, Eleftheriadis K, Virkkula A, Platt A, Förland EJ, Iijima Y, Nielsen IE, Bergin MH, Candlish L, Zimov NS, Zimov SA, O'Neill NT, Fogal PF, Kivi R, Konopleva-Akikh EA, Verlinde J, Kustov VY, Vasel B, Ivakhov VM, Viisanen Y, Intrieri JM (2016) International Arctic systems for observing the atmosphere: an international polar year legacy consortium. *Bull Am Meteorol Soc* 97(6):1033–1056. <https://doi.org/10.1175/BAMS-D-14-00145.1>
- Walsh JE, Overland JE, Groisman PY, Rudolf B (2011) Ongoing climate change in the Arctic. *Ambio* 40(S1):6–16. <https://doi.org/10.1007/s13280-011-0211-z>
- Wang Zhi-Hua, Bou-Zeid E (2012) A novel approach for the estimation of soil ground heat flux. *Agric Forest Meteorol* 154–155:214–221. <https://doi.org/10.1016/j.agrformet.2011.12.001>
- Watanabe K, Mizoguchi M, Kiyosawa H, Kodama Y (2000) Properties and horizons of active layer soils in tundra at Tiksi, Siberia. *J Jpn Soc Hydrol Water Resour* 13(1):9–16. <https://doi.org/10.3178/jjshwr.13.9> (in Japanese)
- Watanabe K, Kiyosawa H, Fukumura K, Ezaki T, Mizoguchi M (2003) Spatial and temporal variation in thaw depth in Siberian tundra near Tiksi. In: Phillips M, Springman SM, Arenson LU (eds) *Permafrost*, Proceedings of the eighth international conference on permafrost, 21–25 July 2003, Zurich, Switzerland, Swets & Zeitlinger, Lisse, pp 1211–1216. http://www.arlis.org/docs/vol11/ICOP/55700698/Pdf/Chapter_213.pdf
- Webb EK, Pearman GI, Leuning R (1980) Correction of flux measurements for density effects due to heat and water vapour transfer. *Q J R Meteorol Soc* 106(447):85–100. <https://doi.org/10.1002/qj.49710644707>
- Whyte LG, Goalen B, Hawari J, Labbe D, Greer CW, Nahir M (2001) Bioremediation treatability assessment of hydrocarbon-contaminated soils from Eureka, Nunavut. *Cold Reg Sci Tech* 32(2–3):121–132. [https://doi.org/10.1016/S0165-232X\(00\)00025-2](https://doi.org/10.1016/S0165-232X(00)00025-2)
- Yang Z, Gao J, Zhao L, Xu X, Ouyang H (2013) Linking thaw depth with soil moisture and plant community composition: effects of permafrost degradation on alpine ecosystem on the Qinghai-Tibet Plateau. *Plant Soil* 367(1):687–700. <https://doi.org/10.1007/s11104-012-1511-1>